First-principles study of boron sheets and nanotubes

Hui Tang and Sohrab Ismail-Beigi
Department of Applied Physics, Yale University, New Haven, Connecticut 06520, USA
(Received 30 April 2010; published 8 September 2010)

Based on first-principles calculations, we present various properties of single- and double-layered boron sheets, along with single- and double-walled boron nanotubes. Single-layered boron sheets, made of hexagons and triangles, have buckled ground-state geometries if the ratio of triangles to hexagons is large and stay flat otherwise. We demonstrate that this asymmetric behavior of buckling cannot be explained by a simple chemical picture based on σ-π mixing. Instead, reduction in the electronic kinetic energy is the driving force for buckling. In addition, we show that double-layered boron sheets can form strong interlayer bonds between two layers only if the precursor single-layered sheet itself prefers a buckled ground-state structure. The optimal double-layered boron sheet in our library is semiconducting and is more stable than any single-layered sheet. Next, we discuss the curvature energies, buckling behavior and soliton structural fluctuations for single-walled boron nanotubes and the implications for the electronic properties of these nanotubes: our main finding is that the semiconducting nature of small-diameter single-walled nanotubes is robust under various perturbations and fluctuations. We end by showing that due to strong bonds forming between walls, the optimal double-walled boron nanotubes have different wall structures from single-walled ones. Such double-walled nanotubes are always more stable than any single-walled nanotube and are furthermore metallic for the likely experimentally relevant diameter range. We conclude with the implications of these results for fabricated nanotube systems.

DOI: 10.1103/PhysRevB.82.115412 PACS number(s): 61.46.−w, 68.65.−k, 73.22.−f, 73.63.Fg

I. INTRODUCTION

The fifth element on the periodic table, boron, occupies an interesting transitional position between nonmetallic and metal elements. Boron compounds exist in the variety of intriguing and peculiar geometric configurations. All the varied phases of pure boron crystals are composed of B_{12} icosahedra but can have complex structures linking these icosahedra to yield primitive unit cells with many atoms.[1–6] While the simplest phase, α rhombohedral boron, has 12 atoms per primitive cell,[1–3] there are approximately 106.67 atoms per primitive cell in the β rhombohedral boron structure.[3,4] One possible rationalization of this complex bonding behavior is that boron is electron deficient so that boron crystals are stabilized by the mixing of two-center and three-center bondings.[1,4]

Similar to boron crystals, nanostructures of boron also exhibit versatile morphology. Small boron clusters tend to form buckled two-dimensional (2D) quasiplanar disklike structures made of triangular motifs[7–15] and are aromatic in the same manner as carbon molecules.[12,16] Large boron clusters with more than 20 atoms prefer to roll up and form ring structures with surfaces composed of triangular motifs.[15,17–19] Based on theoretical and experimental studies on such boron clusters with triangular structural motifs, researchers have predicted the existence of long one-dimensional boron nanotubes.[20–24] In 2004, the first boron nanotubes were fabricated in experiments.[25] Since then, single-walled boron nanotubes have been investigated in many theoretical works using the buckled triangular sheet as the precursor.[26–30] These works predicted that single-walled boron nanotubes are always metallic with large densities of states around their Fermi energies and that the stability of such boron nanotubes depends on both diameter and chirality. Researchers have further shown that double-walled boron nanotubes based on the buckled triangular sheet are more stable than their single-walled counterpart with bonds forming between inner and outer walls.[31]

In 2007, stable boron clusters in the form of boron fullerenes were theoretically predicted.[32] These hollow spherical structures have surfaces composed of mixtures of pentagons, hexagons, and triangles. Structures of these boron fullerenes are closely related to those of carbon fullerenes. For instance, the B_{80} fullerene can be constructed from the C_{60} structure by filling all 20 hexagon faces with extra atoms. Separately, a large class of stable 2D boron sheets were found.[33,34] These boron sheets are made of hexagonal and triangular motifs and are more stable than the buckled triangular sheet. The stability of these boron sheets is explained through a balance between two-center bonding and three-center bonding.[33] These discoveries have spurred further research work: various boron fullerenes have been studied and general design rules to construct stable boron fullerenes and sheets have been proposed;[35–38] small-diameter single-walled boron nanotubes haven been shown to be semiconducting due to surface buckling;[34,39] metal-doped boron fullerenes and nanotubes are proposed to be good candidates for hydrogen storage;[40,41] a route to construct stable metal boride nanostructures has been presented based on a self-doping picture for 2D boron sheets.[38]

In all these works, researchers have found out that surface buckling is a common phenomenon for boron nanostructures. 2D quasiplanar boron clusters are always buckled.[7–15] For 2D boron sheets, some are flat while others tend to have ground-state structures with buckled surfaces, e.g., the buckled triangular sheet.[26,28] Furthermore, although the most stable single-layered boron sheet is metallic, small-diameter single-walled boron nanotubes made from it are semiconducting because of surface buckling.[34,39] Finally, as we describe below in Sec. IV, surface buckling is a critical determining factor for stabilizing double-layered boron sheets. We

believe that clarifying the origin of this universal tendency toward buckling is an important part of understanding the behavior and stability of boron nanostructures. Therefore, our goals are to elucidate this particular issue.

Another important topic not yet thoroughly addressed in the literature is the stability of double-walled boron nanotubes: to date, most studies that we are aware of have focused on single-walled nanotubes. It is an interesting and important question to see whether double-walled (or multiwalled) boron nanotubes are more stable than single-walled ones. As we discuss in Sec. VI, stable double-walled boron nanotubes are possible with properties distinct from single-walled varieties.

The broad aims of this work are to use first-principles theory to address the following: (a) to provide a detailed discussion of the stability of 2D single-layered boron sheets and their buckling behavior, (b) to explain the physical mechanism driving the buckling, (c) to explain the stability and buckling behavior of double-layered boron sheets, (d) to examine the stability and buckling behavior of single-walled boron nanotubes, and (e) to describe the construction, stability, and physical properties of double-walled boron nanotubes.

The paper is organized as follows. In Sec. II we describe our theoretical and computational approach. In Sec. III we present our results on atomically thin boron sheets, describe the asymmetric buckling behavior in this class of boron sheets, and explain the driving force for the buckling. In Sec. IV, we use the knowledge gained from the buckling behavior of single-layered boron sheets to study the structure and stability of double-layered boron sheets which leads us to a particularly stable and semiconducting double-layered boron sheet. In Sec. V, we discuss the properties of single-walled boron nanotubes: their curvature energies, their buckling behavior, the relation of their buckling to their electronic structures and stability, and the role of structural fluctuations on their properties. In Sec. VI, we consider double-walled boron nanotubes constructed in three different ways and compare their relative and absolute stability and their electronic properties to their single-walled cousins. We summarize and conclude in Sec. VII.

II. METHODOLOGY

We calculate the electronic ground-state properties using density-functional theory[42,43] with the *ab initio* pseudopotential total energy approach.[44] Our results are obtained with the local density approximation (LDA) (Refs. 43 and 45) for the exchange and correlation interactions while the generalized gradient approximation (GGA) (Ref. 46) is employed to check key results. Overall, our LDA and GGA results are very similar with some minor quantitative differences. We use norm-conserving pseudopotentials generated by the Troullier-Martins scheme.[47] The pseudopotential for boron is generated with the $2s^2 2p^1 3d^0$ reference configuration, with radial cutoffs $(r_c^s, r_c^p, r_c^d) = (1.7, 2.1, 1.7) a_0$, and the d potential is the local channel. To study boron sheets, supercells are set up to make sheets extended along x-y directions while periodic images along z direction have an distance of 10.6 Å which is sufficient for studying isolated boron sheets. For boron nanotubes, the tubes are extended with periodic boundary conditions along z while the lattice is square in the x-y plane where the distance between the outer walls of adjacent periodic copies of the tubes is at least 10.6 Å to ensure that we study the limit of isolated nanotubes.

We use two different basis sets to deal with systems of different sizes. Two plane wave codes, PARATEC[48] and PWSCF,[49,50] are used for small systems with tens of atoms (mainly boron sheets). A plane-wave-basis set with an energy cutoff of 32 Ry is used to expand the electronic wave functions. For large systems with hundreds of atoms (mainly boron nanotubes), we calculate the ground-state properties with the SIESTA code,[51,52] for which numerical atomic orbitals with double-ζ polarization are used to expand the single-particle wave functions, an equivalent plane-wave cut-off energy 80 Ry is used to construct the real space mesh, and an energy shift of 0.02 Ry is chosen to define the confined localized orbitals. For either approach, K-point sampling for every system converges total energies to better than 1 meV/atom and we use a Gaussian smearing width of 0.05 eV to perform all the K-space integrals. All systems are relaxed until atomic forces are smaller than 0.01 eV/Å and stresses are below 50 MPa. We have checked the results calculated with SIESTA versus PARATEC and PWSCF for small boron sheets and nanotubes. Compared to PARATEC and PWSCF, SIESTA results show the same energetic trend and similar energy differences for various structures in spite of different absolute binding energies. Structures are visualized with the XCRYSDEN code.[53]

III. SINGLE-LAYERED BORON SHEETS

A. Atomically thin single-layered boron sheets

Boron, the neighbor of carbon, displays versatile chemical bonding when compared to carbon. As shown in our previous work,[33] boron sheets, the possible 2D precursors of boron nanotubes, are composed of mixtures of triangular and hexagonal motifs. These sheet structures are stabilized through the balance between two-center bonding in the hexagonal regions and three-center bonding in the triangular regions.[33] Therefore, the stability of boron sheets depends strongly on the ratio of hexagons to triangles, which is described by a "hexagon hole density" η.[33] η changes from 0 to 1/3 as boron sheets alter from the triangular sheet T(0) [see Fig. 3(a)] to the hexagonal sheet H(1/3) [see Fig. 1(b)]. The most stable boron sheet structure, sheet α or A(1/9) [see Fig. 3(c)], occurs at $\eta = 1/9$ due to the fact that electrons fill all the in-plane bonding states and leave all the in-plane antibonding states empty, which results from a prefect balance of two-center bonding and three-center bonding.

In this work, the naming system for boron sheets involves using a letter followed by the η value to designate a single-layered sheet: T(0) is the flat triangular sheet, H(1/3) is the hexagonal sheet and A(1/9) is the most stable α sheet. For double-layered boron sheets discussed mainly in Sec. IV, we name a sheet using the word "double" followed by the name of the corresponding precursor single-layered sheet. For instance, double-B(1/7) refers to a double-layered boron

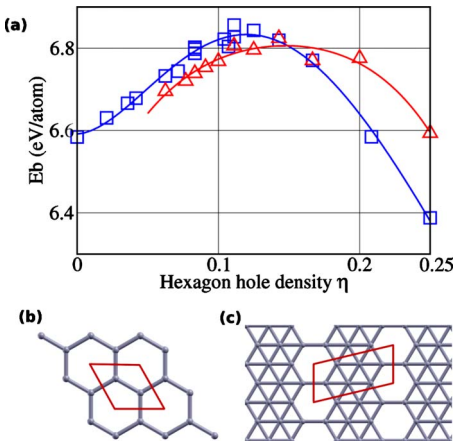

FIG. 1. (Color online) (a) Binding energy E_b (from LDA) versus hexagon hole density η for flat single-layered boron sheets in two extreme cases. The blue "□" are the calculated binding energies for the case where hexagons are evenly distributed. The red "△" are the calculated binding energies for the case where hexagons form lines. The solid curves are polynomial fits to guide the eye. (b) Top view of the hexagonal sheet H(1/3). (c) An example of boron sheets with lines of hexagons. For (b) and (c), the red solid lines show the primitive unit cells. Gray balls are boron atoms and sticks connect nearest-neighbor atoms.

sheet made from stacking two identical B(1/7) sheets [see Fig. 5(b)].

Besides η, the stability of boron sheets also depends on the distribution of hexagons. Full exploration of this degree of freedom obviously leads to an infeasible and combinatorially large search. However, to achieve an understanding of the basic effects, we study the two extremes: either the hexagons are as evenly distributed as possible [e.g., sheet A(1/9)] or the hexagons are packed linearly to form lines [e.g., Fig. 1(c)]. For any sheet, we define the binding energy per atom as

$$E_b = E_{at} - E_{sheet}, \tag{1}$$

where E_{at} is the energy of an isolated spin-polarized boron atom and E_{sheet} is the energy per atom of a sheet. By defining the binding energy this way, larger binding energies correspond to more stable structures.

Figure 1 shows the LDA E_b of flat sheets versus η for both extremes. For even distribution, E_b reaches maximum at $\eta=1/9$ which corresponds to sheet A(1/9). For the linearly aligned hexagons, the most stable structure occurs at $\eta=1/7$, which is 0.03 eV/atom less stable than sheet A(1/9). Although sheets with hexagon lines are more stable for $\eta \geq 1/5$, boron sheets with evenly distributed hexagons are more favorable for η close to 1/9. In this work, since we concentrate primarily on the most stable boron nanostructures, we will be primarily interested in studying the properties of boron sheets with evenly distributed hexagons. In following sections, all boron sheets have hexagons evenly distributed unless noted specifically.

B. Asymmetry of buckling in boron sheets

Unlike graphene, not all 2D atomically thin boron sheets are completely flat. Instead, for many boron sheets, the atoms prefer to move out of the nominal sheet plane and form corrugated surfaces. This phenomenon is generally named "buckling" in the literature. Buckling is quite common in boron nanostructures. All quasiplanar boron clusters studied in both theory and experiments have buckled surfaces.[7–15] For 2D boron sheets made of triangles and hexagons, the ground-state configurations may be either buckled or flat depending on the hexagon-to-triangle ratio (see below). In addition, small-diameter nanotubes have buckled surfaces[34,39] although their precursor, sheet A(1/9), prefers to stay flat. Finally, buckling is closely related to the formation of interlayer bonds in double-layered boron sheets as we discuss in Sec. IV. For these reasons, investigating the buckling of boron sheets is helpful for understanding the basic properties of boron nanostructures.

We have performed a large number of calculations on 2D single-layered boron sheets where we start with flat configurations, create perturbations in the form of buckling of the surfaces, and allow for full relaxations. We summarize the key results here. First, for sheets with $\eta > 1/5$, which in their flat form are already highly unstable compared to the optimal sheets with $\eta \approx 1/9$ (see Fig. 1), we find large vertical buckling amplitudes along the out-of-plane (z) direction and complex resulting final structures. However, even after relaxation, these structures are still quite unstable energetically so we ignore them in what follows. Second, for sheets with $\eta < 1/5$, some sheets buckle vertically along the out-of-plane z direction while some do not and remain flat. More precisely, among boron sheets with evenly distributed hexagons and for $0 < \eta < 1/5$, we find that whether the ground state is buckled or flat depends only on the hexagon hole density η. The buckling behavior is asymmetric with respect to η: sheets with $\eta < 1/9$ prefer to buckle while those with $\eta \geq 1/9$ remain flat. The energetic changes due to buckling are shown in Fig. 2. The increase in stability due to buckling is at most 0.16 eV/atom for the triangular T(0) sheet and decreases to zero as $\eta=1/9$ is approached. The separation point occurs at $\eta=1/9$, which coincides with the optimal sheet structure A(1/9). Therefore, when we account for the buckling effect, the left side ($\eta < 1/9$) of the binding energy curve becomes somewhat flatter as shown in Fig. 2.

It has been known that the triangular sheet T(0) [see Fig. 3(a)] can buckle in many different ways and get trapped in various local minima but the two-atom-cell buckling pattern leads to the most stable structure of the buckled triangular sheet.[26–30,33] However, for other sheets with $0 < \eta < 1/9$, we find that they generally prefer to become buckled in some specific manner. These buckling patterns are determined by the eigenvectors of the unstable phonon modes with imaginary frequencies of the corresponding flat sheets. For instance, the $\eta=1/12$ sheet Z(1/12) shown in Fig. 3(b) has two different buckling patterns determined by its two imaginary phonon modes. One of these patterns is shown in Fig. 3(b) as indicated by coloring. The stabilization of the buckled Z(1/12) sheet is actually quite small and is only 0.01 eV/atom.

On the other hand, the optimal A(1/9) and other sheets with $1/9 < \eta < 1/5$ [e.g., sheets B(1/7) and C(1/6) in Fig. 3]

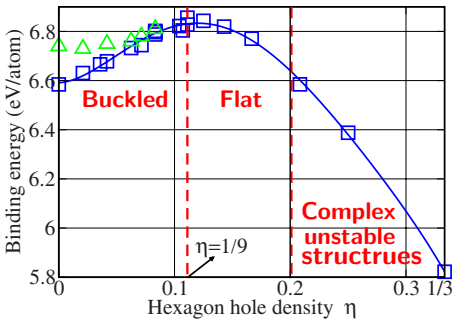

FIG. 2. (Color online) Binding energy E_b (from LDA) versus hexagon hole density η for single-layered boron sheets with evenly distributed hexagons. The blue "□" are the binding energies of flat sheets and the solid blue curve is a polynomial fit. The green "△" are the binding energies for buckled sheets (that are stabilized by buckling). Maximal E_b occurs for sheet α ($\eta=1/9$) or A(1/9), which is the most stable structure. The vertical dashed red line at $\eta=1/9$ indicates the separation point of naturally flat and buckled single-layered boron sheets.

have only stable positive phonon frequencies and thus stay flat. In order to see whether these sheets prefer to buckle when compressed, which is typical when they are bent or curved to form part of a nanotube, we studied these flat sheets under isotropic compression in the x-y plane and checked to see if any phonon became unstable. Not surprisingly, we found that under sufficient compression, every sheet will develop one or more imaginary phonon frequencies and will buckle. For example, sheet B(1/7) has an imaginary phonon frequency once compressed by 5%. The buckling patterns of compressed sheets A(1/9), B(1/7), and E(1/6) are shown in Fig. 3 by coloring.

C. Origin of buckling: σ-π mixing?

What is the origin of this common tendency for 2D boron structures to buckle? An obvious first guess is that perhaps the buckling is driven by mixing of in-plane σ and out-of-plane π states. For a flat 2D structure, all electronic states have either even or odd parity with respect to the reflection in the plane which corresponds to in-plane (σ) and out-of-plane (π) states, respectively. Once a 2D structure becomes buckled, the original reflection symmetry is lost, and in a perturbative picture the resulting electronic states are mixtures of the original in-plane and out-of-plane states. If important mixing happens around the Fermi level, bonding combinations of σ and π states could be pushed below the Fermi level leading to increased stability. (This picture is analogous in many ways to the stabilization coming from a Peierls distortion.) In other words, in this scenario the band energy would decrease sufficiently to overcome the increase in elastic energy and thus make buckling preferable.

Following this idea, the fact that sheet A(1/9) is flat can be rationalized via a simple argument: no mixing between in-plane and out-of-plane states exists around the Fermi energy because the Fermi level lies in an energy gap for the in-plane states.[33] Thus there is no energy gain to compensate the increase of elastic energy. However, this explanation is already

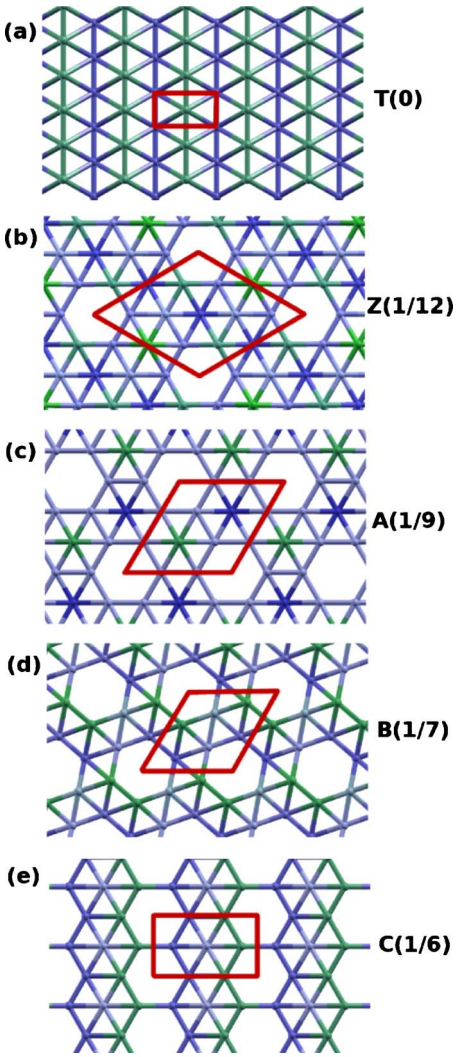

FIG. 3. (Color online) Structures of five boron sheets: (a) T(0), (b) Z(1/12), (c) A(1/9), (d) B(1/7), and (e) C(1/6). The red solid lines show the unit cells. The preferred buckling patterns are indicated by coloring: z coordinates increase as color changes from green to gray to purple so that green means negative z coordinates, gray shows z coordinates close to 0, and blue means positive z. Since the sheets A(1/9), B(1/7), and C(1/6) do not buckle at equilibrium, the buckling patterns shown here are obtained by applying an isotropic compressive strain of 5% in the x-y plane.

problematic because it does not provide a reason for the clear asymmetry in buckling behavior around $\eta=1/9$. All sheets with η above and below 1/9 have in-plane and out-of-plane states coexisting at the Fermi energies so that we would have expected that sheets on both sides of $\eta=1/9$ would buckle in disagreement with the *ab initio* results.

A more careful examination shows that in fact the entire picture is quantitatively incorrect. (A better explanation is provided in the next section.) To examine whether the behavior of the band energy can explain the buckling, we divide the total energy E_{tot} into two parts, the band energy E_{band} and the remainder as a "repulsive" term E_{rep}

$$E_{tot} = E_{band} + E_{rep}, \tag{2}$$

where

TABLE I. Band energies (E_{band}), repulsive energies (E_{rep}), and total energies (E_{tot}) of five boron sheets T(0), Z(1/12), A(1/9), B(1/7), and C(1/6), respectively, for flat and buckled cases (from LDA). For the flat sheets, the energies are in eV/atom. For the buckled sheets, the percentage change from the flat energy is reported to highlight the direction of the energy change ("+" for increase and "–" for decrease). The buckling height is fixed at 0.16 Å in all cases.

	Flat			Buckled		
Sheet	E_{band}	E_{rep}	E_{tot}	δE_{band}	δE_{rep}	δE_{tot}
T(0)	−37.82	8.50	−29.32	+0.89	−4.31	−0.10
Z(1/12)	−37.21	7.68	−29.54	+1.19	−5.81	−0.01
A(1/9)	−36.21	6.61	−29.59	+0.59	−3.18	+0.01
B(1/7)	−35.07	5.52	−29.55	+0.92	−5.00	+0.02
C(1/6)	−33.89	4.38	−29.51	−0.02	+0.68	+0.01

$$E_{band} = \int_{-\infty}^{E_F} D(E) E dE, \tag{3}$$

where $D(E)$ is the electronic density of states and E_F is the Fermi energy, and we compute this energy directly from the first-principles results. The repulsive energy, $E_{rep}=E_{tot}-E_{band}$, is defined and computed exactly as this difference from *ab initio* calculations. (To make E_{rep} always positive, we have defined the repulsive energy of an isolated boron atom to be zero, then E_{rep} and E_{tot} for all boron sheets are scaled accordingly.) As expected from simple tight-binding theory, E_{rep} is generically positive and in a tight-binding picture would be given by a sum over repulsive pair interactions[54]

$$E_{rep} \approx \sum_{R_i,R_j} V(|R_i - R_j|), \tag{4}$$

where $V(|R_i-R_j|)$ is a short-range repulsive interaction between two nuclei at R_i and R_j. (However, we emphasize that we do not use this approximate form but instead compute E_{tot}, E_{band}, and E_{rep} directly from the first-principles results.)

When computing the band energy, it is clear that any shifts in E_F will modify the computed value. It is well known that standard periodic supercell calculations have an arbitrary, and difficult to compute, energy shift stemming from the long-range Coulomb interaction. Therefore, to get reliable E_{band} energies, we must measure E_F with respect to the vacuum level. This is accomplished by performing a series of calculations with differing supercell sizes L along the z direction; the behavior of E_F versus L for large L is essentially linear in L^{-1}. In this way, we can extrapolate to $L=\infty$ and find absolute E_F and thus E_{band} energies.

In the σ-π mixing picture described above, the band energy E_{band} should decrease upon buckling as hybridization around E_F pushes states below E_F. In Table I, we show the calculated band energies and repulsive energies of five sheets spanning a range of η values when they are flat and slightly buckled (according to their preferred buckling patterns), respectively. We can see that all sheets except sheet C(1/6) have their band energies increase and repulsive energies decrease due to buckling, while sheet C(1/6), which naturally does not prefer to buckle, has the opposite behavior. These results are clearly opposite to the expectations from the σ-π mixing picture. In other words, splitting the total energy into band and repulsive energies has not helped us understand the origin of the buckling.

D. Kinetic energy: The driving force for buckling

As the chemical bonding picture based on σ-π hybridization fails to explain the buckling, we turn to a different physical picture. We instead view these 2D metallic boron sheets as a realization of (a possibly nonstandard) 2D electron gas. Namely, we should consider breaking up the total energy into terms that are most natural for an electron gas analysis: the kinetic energy, the (classical) electrostatic energy of interaction among all charges, and the exchange-correlation energy due to the quantum behavior of the electrons. Interestingly, even though 2D boron sheets show significant covalent bonding character, this picture turns out to work well: the kinetic term is dominant, as expected for a medium-to-high-density electron gas, and its variations largely dictate the buckling. Therefore, we write the total energy E_{tot} as

$$E_{tot} = E_{kin} + E_{xc} + E_{es}, \tag{5}$$

where E_{kin} is the total electronic Kohn-Sham kinetic energy, E_{xc} is the exchange-correlation energy (here evaluated within the LDA or GGA), and E_{es} is the sum of all remaining energies. E_{es} physically represents the sum of all classical electrostatic interactions among charges: electron-electron, electron-ion, and ion-ion. (The nonlocal electron-ion interaction from the pseudopotential is thus included in E_{es} as this term is designed to reproduce the interactions of the valence electrons with the nucleus in an all-electron framework.)

Separately, it is helpful to have a measure of the average electron density in the system in order to correlate with usual notions of electron gas behavior. Unfortunately, there is no obvious unique *a priori* way to define an average electron density for an arbitrary material system with a spatially varying electron density. Therefore, we resort to a very simple definition which uses the density itself as the weighing function

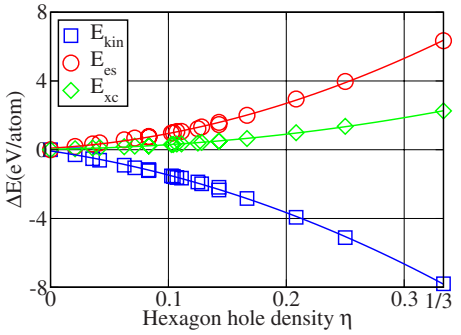

FIG. 4. (Color online) Kinetic (E_{kin}), electrostatic (E_{es}), and exchange-correlation (E_{xc}) energies versus η for flat 2D boron sheets. Energies are in the units of eV/atom. All three energies are plotted with respect to their respective values at $\eta=0$ (the zero of energy). The squares, circles, and diamonds are the calculated results while the solid curves are guides to the eye.

$$\bar{n} = \frac{\int [n(r)]^2 dr}{\int n(r) dr}. \tag{6}$$

This simple measure averages the density in the spatial regions where the electrons spend the most time. Therefore, it is biased to large values by the relatively large values of the electron density close to each boron atom and does not only measure the electron density of the delocalized mobile electrons. However, for our purposes, it is a reasonable definition in which it shows monotonic behavior versus η (see below).

We first investigate how E_{kin}, E_{xc}, and E_{es} behave for flat sheets. Figure 4 shows E_{kin}, E_{xc}, and E_{es} versus η for a large set of flat 2D boron sheets. We can see that E_{kin}, E_{xc}, and E_{es} all change smoothly and monotonically with η or equivalently with $1-\eta$. Because the nearest neighbor distances in the different boron sheets are almost identical,[33] for these flat sheets $1-\eta$ also changes monotonically with the average electron density $\bar{n}$ as shown in Table II. Hence, E_{kin}, E_{xc}, and E_{es} all change monotonically with $\bar{n}$ as one would expect for an electron gas.

We now turn to the buckling effect for these sheets. Table II shows how E_{kin}, E_{xc}, and E_{es} change when each sheet buckles. For the five sheets investigated, E_{kin} always decreases and E_{xc} and E_{es} always increase due to buckling. For those sheets that prefer to buckle, sheets T(0) and Z(1/12) in Table II, the decrease in E_{kin} dominates over the other two energy increases. Therefore, the buckling is driven by kinetic energy lowering and that kinetic energy lowering wins over the increase of $E_{es}+E_{xc}$ for $\eta<1/9$. In addition, we see that $\bar{n}$ is decreased by buckling, and lowering of density is consistent with lowering of kinetic energy (a smaller Fermi momentum or Fermi energy) and higher E_{es} and E_{xc} (larger average charge separation). Intuitively, if we view the sheet as a continuous film, then surface buckling can be expected to increase the surface area which then rationalizes the decrease in electron density: the same number of electrons are spread over a sheet with increased surface area due to the corrugation. However, since there is no rigorous definition of surface area at the discrete atomic scale, this picture serves primarily as an aide to understanding and visualization.

What we have found is that buckling reduces the electron density which in turn lowers the kinetic energy and thus drives the buckling. The kinetic energy is larger and more dominant for higher electron densities (smaller η) so that those sheets will have a stronger tendency to buckle. Most importantly, this picture naturally explains the asymmetry in the buckling behavior about $\eta=1/9$. Since buckling reduces $\bar{n}$, and $\bar{n}$ and $1-\eta$ are in monotonic relation, decreasing $\bar{n}$ effectively increases η. Because the binding energy versus η (see Fig. 1) has a maximum at $\eta=1/9$, sheets with $\eta<1/9$ can increase their stability by buckling while those with $\eta>1/9$ would decrease their stability if they buckled.

The above results clearly show that it is the lowering of the kinetic energy that drives the initial stages of buckling in boron sheets. We may wonder if this finding is more general. After all, for the small buckling amplitudes used above, it can be argued that the geometry and chemical bonding modes barely change but in the final fully buckled structure this may not be the case. For example, the fully buckled triangular sheet has strong two-center-type bonding and the bond length along that direction are significantly reduced[26,27] pointing to basic changes in bonding topology and possibly a decrease in surface area in the intuitive picture above. How-

TABLE II. Kinetic energy (E_{kin}), electrostatic energy (E_{es}), exchange-correlation energy (E_{xc}), total energy (E_{tot}), and the average electron density $\bar{n}$ of five boron sheets T(0), Z(1/12), A(1/9), B(1/7), and C(1/6), respectively, for flat, artificially buckled and fully relaxed cases (from LDA). For flat sheets, energies are in eV/atom and $\bar{n}$ is in units of 10^{-2} e/Bohr^3. For buckled and fully relaxed sheets, we show percentage changes of the energies and $\bar{n}$ compared to the flat values (+ for increase, − for decrease). The buckling height is fixed at 0.16 Å in all artificially buckled sheets.

	Flat					Buckled					Fully relaxed				
Sheet	E_{kin}	E_{es}	E_{xc}	E_{tot}	$\bar{n}$	δE_{kin}	δE_{es}	δE_{xc}	δE_{tot}	$\delta\bar{n}$	δE_{kin}	δE_{es}	δE_{xc}	δE_{tot}	$\delta\bar{n}$
T(0)	57.34	−104.22	−30.12	−77.00	8.85	−1.62	+0.65	+0.74	−0.10	−2.49	−4.10	+1.74	+1.31	−0.20	−3.73
Z(1/12)	56.17	−103.49	−29.90	−77.22	8.74	−0.80	+0.33	+0.35	−0.01	−1.14	−0.44	+0.19	+0.13	−0.01	−0.42
A(1/9)	55.79	−103.25	−29.81	−77.27	8.71	−0.27	+0.11	+0.12	+0.01	−0.46					
B(1/7)	55.16	−102.76	−29.63	−77.23	8.59	−1.34	+0.57	+0.69	+0.02	−2.33					
C(1/6)	54.50	−102.22	−29.47	−77.19	8.47	−0.78	+0.31	+0.43	+0.01	−1.42					

ever, our results show that even in fully relaxed buckled sheets, the kinetic energy is still the energetic driving force: Table II shows that for the triangular T(0) and the Z(1/12) sheets, the kinetic energy and average electron density are always lowered compared to their flat counterparts—and this holds for other sheets we have investigated. Furthermore, as we will show in Sec.V B, the same kinetic energy reduction holds for buckled single-walled boron nanotubes as well. Therefore, we believe that kinetic energy reduction is most probably the key driving force for the buckling of boron sheets and nanotubes.

IV. DOUBLE-LAYERED BORON SHEETS

For boron nanostructures, strong interlayer bonds can be formed between two planar or quasiplanar parts stacking perpendicular to the nominal structure plane.[31,55] Due to these interlayer bonds, multilayered boron sheets can be more energetically favorable than the most stable single-layered boron sheet A(1/9) (see below). When creating boron nanostructures such as nanotubes by folding, wrapping, or cutting boron sheets, it is possible that multilayered boron sheets will be the parent structures under certain growth conditions. Therefore, studying multilayered boron sheets, where the simplest cases are those of double-layered sheets, can be relevant to understanding experimentally grown structures as well as to helping us understand the general properties for boron nanostructures.

Below, we find that the knowledge we have gained (above) concerning the buckling of single-layered boron sheets is invaluable in clarifying and rationalizing the tendencies for buckling and formation of interlayer bonds in double-layered systems. In this work, we limit ourselves to double-layered sheets which already create a large class of systems to study and analyze. Our primary aim is to obtain a basic understanding of the buckling and bonding behavior of boron sheets when they are in close proximity. An extension of these results to multilayered structures is beyond the scope of the present work.

To study double-layered boron sheets, we proceed in the following manner: we take two (primitive cell) copies of a particular 2D boron sheet and place the two copies some initial distance apart (≈3 Å). We then create some random perturbations of all atomic positions and perform a full relaxation. After following this procedure for a large number of such double-layered structures, we discover that a pair of sheets with $\eta < 1/9$ tend to make strong interlayer bonds. On the other hand, two sheets with $\eta \geq 1/9$ do not: the two single-layered sheets stay quite flat, are weakly bound, and stay apart at a relatively large distance of typically 3.5–3.6 Å. (This separation likely correlates with weak van der Waals interactions which are not correctly captured by LDA or GGA calculations; however, our main point is that the interactions are quite weak and no interlayer bonds are formed which we believe is a robust result even if van der Waals interactions were included correctly.) Two typical examples are shown in Fig. 5. When interlayer bonds form, the interlayer bond length is about 1.7 Å which is quite typical of the lengths in 2D boron structures.

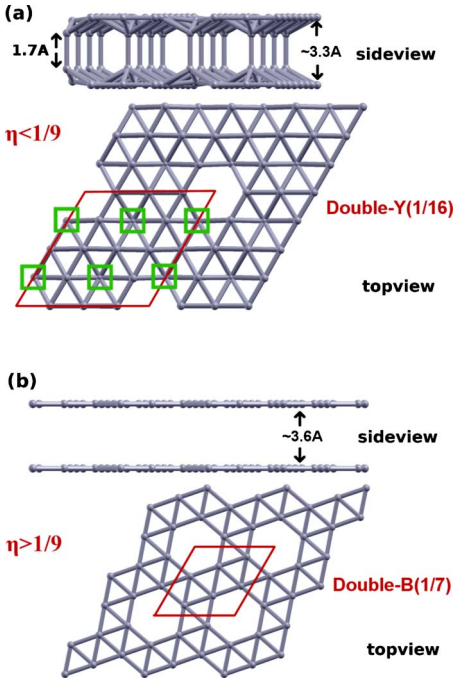

FIG. 5. (Color online) Illustration of structures of double-layered boron sheets (top and side views) for both (a) the $\eta < 1/9$ double-Y(1/16) sheet and (b) the $\eta > 1/9$ double B(1/7) sheet. The red solid lines in the top views show the 2D primitive unit cells. The green squares in the top view of (a) mark the atoms that form interlayer bonds in a primitive cell.

The above behavior is simply explained from buckling behavior of single-layered boron sheets: a pair of sheets will form interlayer bonds only when each sheet alone prefers to buckle in the first place (i.e., both sheets have $\eta < 1/9$). The main requirement is to properly align the sheets so that the geometry allows the buckling atoms to make interlayer bonds with each other. As a simple further test of the relation between buckling and formation of interlayer bonds, we know that the optimally stable A(1/9) sheet does not normally buckle but can be forced to buckle when under compression. Therefore, we put 1% of isotropic compression in the *xy* plane on a pair of A(1/9) sheets in close proximity and find that the sheets buckle, that they form interlayer bonds of about 1.7 Å in length, and that the bonding pattern is the one dictated by the buckling pattern of the single-layered sheet under compression (see Fig. 3).

Table III shows a subset of our *ab initio* results for double-layered boron sheets built from pairs of T(0), Y(1/16), Z(1/12), A(1/9), and B(1/7) sheets. The first three double-layered sheets, made from T(0), Y(1/16), and Z(1/12), form interlayer bonds with the bond lengths close to 1.7 Å and thus strongly stabilize (i.e., bind) the double-layer system. The energy reduction due to the interlayer bonding, E_{bond} in the Table, is significant and gets larger for smaller η since more interlayer bonds form. As a result, we find that the most stable double-layered sheet in our library occurs at $\eta = 1/12$ for the double-Z(1/12) case. This double-layered system is 0.135 eV/atom more stable than the optimal single-layered A(1/9) sheet and is the most stable sheet structure we have found to date. Figure 6 shows the atomic structure and

TABLE III. Energetic and geometric properties of five double-layered boron sheets constructed from pairs of T(0), Y(1/16), Z(1/12), A(1/9) and B(1/7) sheets (from LDA). The first three double-layer sheets form interlayer bonds while the other two do not. E_{bond} (in eV/atom) is the reduction in energy (i.e., binding energy) of the double-layer sheet compared to the two separate constituent single-layer sheets. d_{bond} (in Å) is the interlayer bond length. N_{bond} is the number of interlayer bonds per atom formed between the two sheets. ΔE_α (in eV/atom) is the energy of the double-layer system compared to the optimal single-layered A(1/9) (α) sheet. d_{inter} (in Å) is the distance between two nominal sheet planes defined by boron atoms not making interlayer bonds.

Sheets	η	E_{bond}	d_{bond}	N_{bond}	ΔE_α	d_{inter}
T(0)	0	−0.30	1.70	1/8	−0.03	3.37
Y(1/16)	1/16	−0.24	1.70	4/30	−0.12	3.33
Z(1/12)	1/12	−0.19	1.69	3/22	−0.135	3.23
A(1/9)	1/9	−0.02		0	−0.02	3.49
B(1/7)	1/7	−0.03		0	+0.01	3.60

the electronic band structure of the double-Z(1/12) sheet. In contrast to the single-layered sheets which are all metallic, the double-Z(1/12) sheet is semiconducting with a reasonably large LDA band gap of 0.8 eV. Speaking figuratively, the formation of the interlayer bonds has created bonding and antibonding combinations of the states that used to be at the Fermi level, pushed them above and below the Fermi level, and thus created a semiconducting system. Due to its stability, boron nanotubes could in fact originate from this double-Z(1/12) sheet. However, depending on growth conditions during experiment, it might be possible that either single or double layered tubes will be preferred, thus making the nanotubes either metallic or semiconducting. Some of the aspects addressable from first principles are discussed in the following sections.

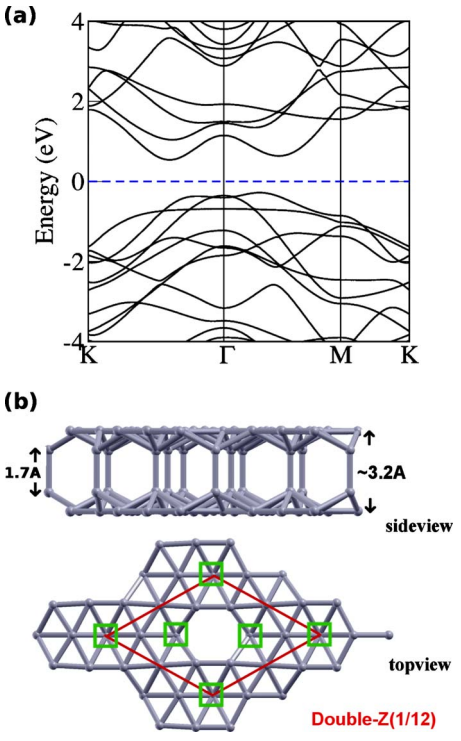

FIG. 6. (Color online) (a) Band structure of the double-Z(1/12) sheet: the Fermi level is set to zero, which is illustrated by the blue dashed line. (b) Structure of the double-Z(1/12) sheet (side view and top view). Red solid lines show the unit cell and green squares mark the atoms making interlayer bonds in one unit cell.

V. SINGLE-WALLED BORON NANOTUBES

We now turn to single-walled nanotubes made from single-layered 2D boron sheets, and we investigate primarily their curvature energies and surface buckling. We name a boron nanotube (single walled or double walled) following the established standard for carbon nanotubes: an (n,m) nanotube has its chiral vector $Ch=n\times\boldsymbol{a}_1+m\times\boldsymbol{a}_2$, where $\boldsymbol{a}_1$ and $\boldsymbol{a}_2$ are the two primitive lattice vectors of the corresponding sheet structure.[56] We take the extended direction of the nanotube to be along the z direction. The curvature energy of a nanotube, E_{curv}, is defined as

$$E_{curv} = E_{tube} - E_{sheet}, \tag{7}$$

where E_{tube} is the energy per atom of that nanotube and E_{sheet} is the energy per atom of the corresponding sheet structure. Therefore, E_{curv} is the energy cost of rolling up the sheet into a tubular structure.

A priori, the number of possible structures for single-walled nanotubes is enormous. However, we know that the A(1/9) sheet is the most stable 2D single-layered boron sheet, so that for large diameter nanotubes with vanishing curvature, we are assured that surface structure of the most stable single-walled nanotubes will be that of the A(1/9) structure. Based on this fact, we simply constrain all the single-walled nanotubes we study to be built from the A(1/9) structure regardless of diameter. In principle, one can investigate the question of whether single-walled nanotubes made from sheets other than A(1/9) might be stabilized due to curvature effects for small diameters but this question is beyond the scope of our present work.

The optimal boron sheet A(1/9) has a energy gap for the in-plane σ states and a finite density of states for the out-of-plane π manifold.[33,34] Thus, the conductivity of the A(1/9) sheet comes only from out-of-plane π states. Therefore, large-diameter single-walled nanotubes built from A(1/9)

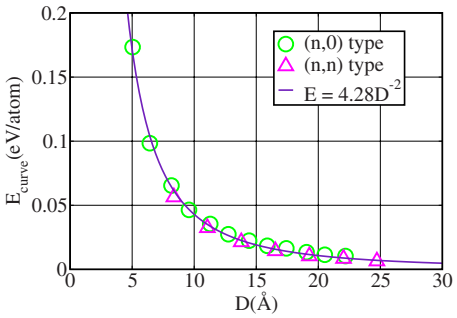

FIG. 7. (Color online) Curvature energies E_{curv} in eV/atom of single-walled boron nanotubes made of the A(1/9) sheet versus diameter D in Å (from LDA). Green "○" are for $(n,0)$ nanotubes with n ranging from 3 to 14. Magenta △ are for (n,n) nanotubes with n ranging from 3 to 9. The indigo solid line is a single-parameter $1/D^2$ fit to the combined data set.

will always be metallic since the electronic structures are determined by the zone-folding technique.[56,57] However, it has been found that small-diameter boron nanotubes built from the A(1/9) sheet are semiconducting, with energy gaps around a few tenth of eVs, due to curvature and surface buckling.[34,39] Below, we investigate in detail these curvature effects on the energetics and electronic structures of the single-walled nanotubes.

A. Curvature energy

Figure 7 shows how the curvature energy E_{curv} changes with tube diameter D for a wide range of such achiral single-walled nanotubes [i.e., $(n,0)$ and (n,n) nanotubes] created from wrapping the A(1/9) sheet. The data from these two different classes of nanotubes lie almost exactly on the same smooth curve, suggesting that the curvature energy of this type of single-walled nanotubes does not depend strongly on chirality. Namely, E_{curv} is determined by the nanotube diameter D, a result that is consistent with previous works on this problem.[34,39]

As is the case for carbon nanotubes,[58,59] we expect from elastic theory that E_{curv} should have the following simple dependence on D for large D:

$$E_{curv} = \frac{C}{D^2}, \tag{8}$$

where C is a constant. By fitting all the data in Fig. 7, we obtain $C=4.28$ eV Å^2/atom, slightly larger than the value $C=3.64$ eV Å^2/atom in previous work,[39] which we believe is due to the fact that the LDA we use usually results in stronger bonding than GGA-PBE (Ref. 46). For comparison, carbon nanotubes have $C=8.56$ eV Å^2/atom.[58,59] Therefore, for a given diameter, it is easier to curve the A(1/9) sheet than to curve graphene to create single-walled nanotubes.

B. Surface buckling under large curvature

Since sheet A(1/9) is metallic with a large density of states at its Fermi energy coming from the out-of-plane π manifold, simple zone folding leads us to expect that all

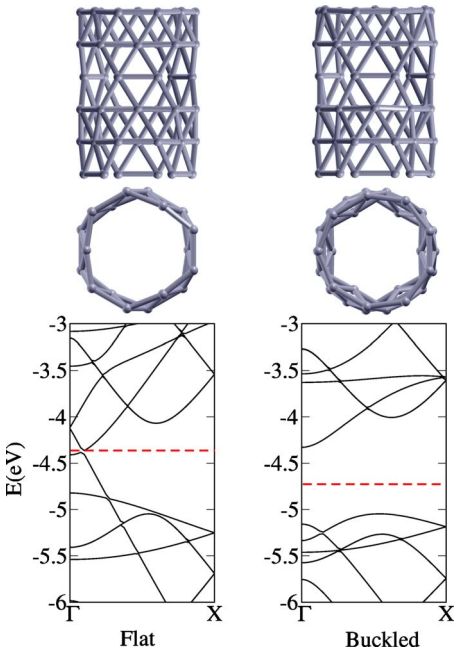

FIG. 8. (Color online) Structures (side view and top view) and band structures of the single-walled boron nanotube (3,0) with flat (left) and buckled (right) surfaces (from LDA). Red dashed lines show the Fermi energies.

boron nanotubes made of sheet A(1/9) are metallic. However, boron nanotubes with small radii are actually semiconducting due to the fact that tube surfaces become buckled under the large curvature necessitated by the small diameter. This buckling has been attributed to rehybridization in the σ-π manifold.[34,39]

As we explained in Sec. III B, sheet A(1/9) prefers to stay flat when it is stress free but will buckle under compression. When it buckles, the two boron atoms in each unit cell that are in the triangular regions will move out of the sheet plane with one going up and the other going down (see Fig. 3). We find that when the A(1/9) sheet is curved to form nanotubes, the same buckling pattern is observed: the two atoms in the triangular regions become inequivalent with one moving radially inward and the other moving radially outward. Due to this surface buckling, small-diameter single-walled boron nanotubes become semiconducting. Figure 8 shows the single-walled nanotube (3,0) as an example. This buckling and semiconducting behavior is only relevant for small diameter nanotubes: as Fig. 9 shows, the band gap vanishes for diameters larger than ~20 Å.[34,39] We also see that for a fixed diameter, the band gaps for $(n,0)$ and (n,n) nanotubes can be significantly different.

As our results in Fig. 9 show, the LDA and GGA result in systematically different band gaps for these single-walled boron nanotubes with results that differ by ~0.1–0.2 eV for the same nanotube index. However, since LDA and GGA give very similar band-gap predictions for bulk materials, the difference is most likely not due to the treatment of exchange correlation but instead coming from a structural difference. In fact, the GGA generally predicts a larger surface buckling for single-walled nanotubes than LDA (see Table V). Therefore, we plot the same data versus the buckling amplitude

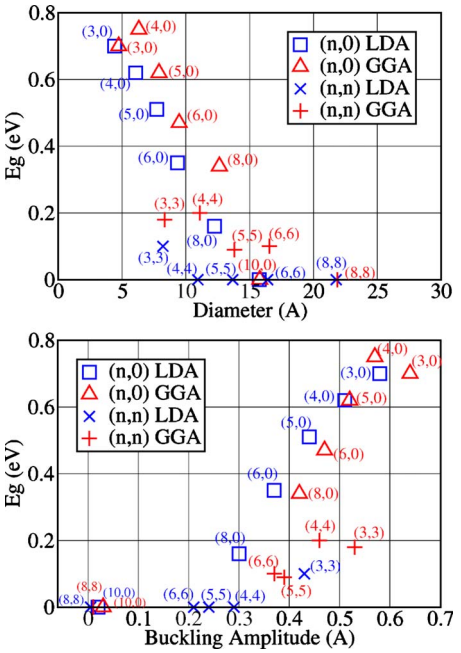

FIG. 9. (Color online) Band gap E_g (in eV) versus tube diameter (top, in Å) and buckling amount (bottom, in Å) for $(n,0)$- and (n,n)-type A(1/9)-derived single-walled boron nanotubes calculated with both LDA and GGA.

instead of diameter in Fig. 9—the buckling amplitude is the difference in radial distance of the two types of buckled triangular atoms. We see an approximate collapse of the data on a single curve for both $(n,0)$ and (n,n) nanotubes. Therefore, we believe that to leading order, the band gap for a single-walled nanotube is determined by its buckling amplitude, while the relation of the buckling amplitude to the diameter is more complex but secondary.

To understand the surface buckling in more detail, we have compared the properties of the buckled ground state of a single-walled nanotube to the same nanotube but with a flat surface. The flat structure is constructed as follows: we know that the atoms that buckle are those corresponding to the atoms of the parent A(1/9) sheet that are in a triangular region. The symmetry breaking leading to the ground state has one of these atoms move inward and the other move outward. To generate the flat structure, we simply force these two atoms to remain equivalent by doing a constrained atomic relaxation whereby we constrain these two atoms to have the same radius measured from the nanotube axis. As expected, for flat surfaces, the single-walled boron nanotubes are all metallic regardless of diameter [e.g., see (3,0) nanotube in Fig. 8]. Table IV shows the changes in different components of the total energy of buckled single-walled boron nanotubes compared to flat ones. For all nanotubes, buckling is always accompanied by a decrease in kinetic energy E_{kin} and increases in E_{xc} and E_{es}, the same as for 2D boron sheets. This strongly suggests that surface buckling in single-walled boron nanotubes is also driven by lowering of kinetic energy.

The total energy differences between flat and buckled nanotubes are found in Tables IV and V. The energy differences per atom are extremely small and decrease to zero rapidly with increasing nanotube diameter: they are at most 15 meV/atom for the smallest diameters. We note that the GGA systematically favors buckled surfaces compared to the LDA and predicts larger energy gains from buckling. Given the extremely small magnitude of these energy differences, it is not clear whether the LDA or GGA is accurate enough to capture them correctly. In fact, a recent work[60] has investigated the geometry of a finite (5,0) single-walled boron nanotube segment using the presumably more accurate MP2 method[61] and concluded that no buckling exists on the surface of this finite nanotube because the buckled configuration has a higher energy. This is in contrast to our results here and previous LDA- and GGA-based findings.[34,39] Hence, we believe that more caution is required regarding the LDA/GGA

TABLE IV. Kinetic energy (E_{kin}), exchange-correlation energy (E_{xc}), electrostatic energy (E_{es}), total energy (E_{tot}) for flat- and buckled-surfaced single-walled boron nanotubes made of sheet A(1/9) based on LDA calculations using SIESTA. For flat cases, energies are in eV/atom. For buckled ones, we show percentage changes of the energies compared to the corresponding flat values (+ for increase, − for decrease).

	Flat-surfaced				Buckled-surfaced			
Tube	E_{kin}	E_{xc}	E_{es}	E_{tot}	δE_{kin}	δE_{xc}	δE_{es}	δE_{tot}
(3,3)	54.90	−29.74	−102.16	−77.00	−0.14	0.05	0.06	−0.007
(4,4)	54.99	−29.76	−102.25	−77.02	−0.09	0.03	0.04	−0.004
(5,5)	55.06	−29.78	−102.31	−77.03	−0.09	0.03	0.04	−0.002
(6,6)	55.05	−29.78	−102.31	−77.04	−0.07	0.02	0.03	−0.001
(8,8)	55.18	−29.82	−102.41	−77.05	−0.28	0.16	0.11	0
(3,0)	54.73	−29.68	−101.92	−76.87	−0.28	0.10	0.11	−0.013
(4,0)	54.86	−29.72	−102.09	−76.95	−0.22	0.06	0.09	−0.009
(5,0)	54.92	−29.74	−102.17	−76.98	−0.19	0.05	0.08	−0.007
(6,0)	54.99	−29.76	−102.24	−77.01	−0.18	0.06	0.08	−0.004
(8,0)	55.03	−29.77	−102.29	−77.03	−0.14	0.05	0.06	−0.001
(10,0)	55.06	−29.78	−102.32	−77.04	−0.01	0.00	0.01	0

TABLE V. Energetic, structural, and electronic data for $(n,0)$- and (n,n)-type single-walled boron nanotubes derived from sheet A(1/9) based on LDA and GGA calculations. The table shows total energy differences δE (in meV/atom) between flat- and buckled-surfaced cases of a nanotube, (average) nanotube diameter D (in Å), buckling amplitude A_{buckle} (in Å), and the nanotube band gap E_{gap} (in eV).

	LDA				GGA			
Tube	δE	D	A_{buckle}	E_{gap}	δE	D	A_{buckle}	E_{gap}
(3,3)	2.71	8.20	0.43	0.10	6.57	8.3	0.53	0.18
(4,4)	1.30	10.9	0.29	0	4.19	11.1	0.46	0.20
(5,5)	0.68	13.7	0.24	0	2.73	13.8	0.39	0.09
(6,6)	0.35	16.4	0.21	0	1.95	16.5	0.37	0.10
(8,8)	0.32	21.8	0.01	0	1.39	21.9	0.01	0
(3,0)	9.81	4.40	0.58	0.70	14.85	4.73	0.64	0.70
(4,0)	7.16	6.06	0.51	0.62	11.38	6.31	0.57	0.75
(5,0)	5.12	7.70	0.44	0.51	8.86	7.89	0.52	0.62
(6,0)	3.13	9.33	0.37	0.35	6.32	9.47	0.47	0.47
(8,0)	0.50	12.2	0.30	0.16	3.88	12.6	0.42	0.34
(10,0)	0.03	15.7	0.02	0	2.29	15.8	0.03	0

predictions for such small energy differences and that further studies are required to determine the correct ground-state geometries and electronic properties of single-walled boron nanotubes made from the A(1/9) sheet. However, if surface buckling does in fact take place, the generic monotonic trend of decreasing buckling and decreasing gap with increasing diameter is most likely a robust result. In the next section, we discuss fluctuations in surface buckling assuming that the LDA/GGA predictions for the buckling are valid.

C. Fluctuations in buckling

The fact that small diameter nanotubes constructed from the A(1/9) sheet are semiconducting is a symmetry breaking phenomenon: the surface of the nanotube buckles in a way that two originally equivalent atoms (per surface unit cell) become inequivalent whereby one moves radially inwards and the other outward. The existence of two distinct but symmetry-related minima, i.e., a degenerate ground state, allows for the possibility of topological soliton fluctuations at finite temperatures that connect one minimum to the other. A topological soliton represents a stable, nonuniform distribution of an order parameter (surface buckling here) that occurs in a system with several degenerate ground-state configurations: the soliton connects two regions of the system which lie in distinct minima; topological solitons are stable and cannot easily decay because no continuous transformation can map the system back to a trivial uniform distribution in a single minimum.[62] Because the region of the soliton joining the two minima will have a relatively flat nanotube surface, it will be metallic and thus the nanotubes will have semiconducting regions separated by metallic islands. We examine the likelihood of this possibility below: the main motivation is that the energy difference between flat and buckled configurations is quite small so thermal fluctuations might play an important role.

Figures 10 and 11 show typical results for the energy and band gap of (3,0) and (5,0) nanotubes as a function of buckling amplitude. Figure 12 shows the structure of the buckled (5,0) nanotube and also identifies the atoms undergoing the buckling motion. For intermediate buckling amplitudes, the ground-state buckled configuration and the flat configuration are used as end points, and the intermediate configurations are linearly interpolated between them. The reflection symmetry of the plots in Fig. 10 and 11 is a consequence of the symmetry breaking in the system. The band gap versus buck-

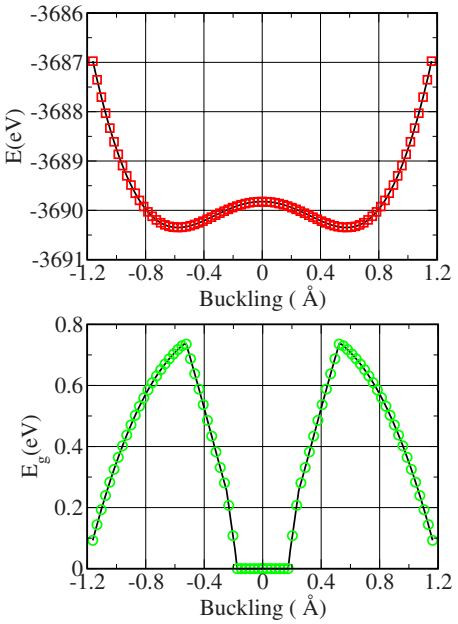

FIG. 10. (Color online) Total energy per nanotube primitive cell (top, in eV) and band gap (bottom, in eV) versus buckling amplitude (in Å) for the 48-atom primitive cell of the single-walled boron nanotubes (3,0) (from LDA). Red squares and green circles are the calculated data. Black solid curves are guides to the eye.

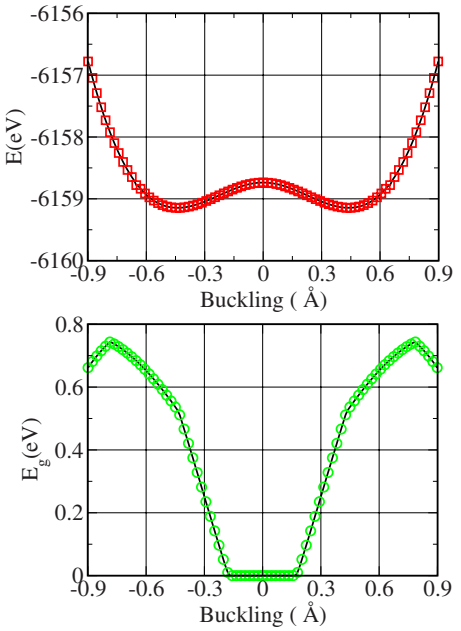

FIG. 11. (Color online) Total energy per nanotube primitive cell (top, in eV) and band gap (bottom, in eV) versus buckling amplitude (in Å) for the 80-atom primitive cell of the single-walled boron nanotubes (5,0) (from LDA). Red squares and green circles are the calculated data. Black solid curves are guides to the eye.

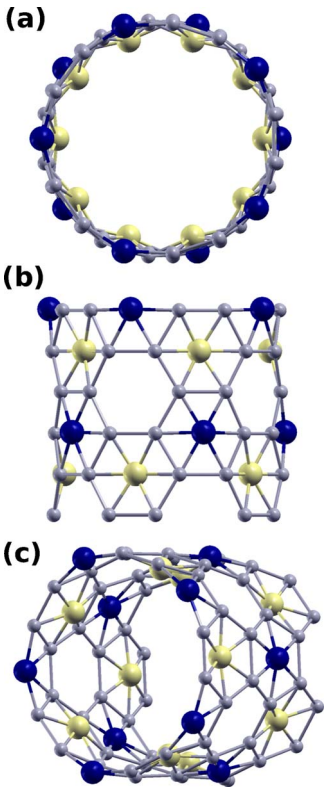

FIG. 12. (Color online) Structure of the (5,0) single-walled boron nanotube: (a) top view, (b) side view, and (c) angled view. Big blue (dark) balls are the boron atoms moving outward, big yellow (light) balls show the atoms moving inward, and small gray balls show the rest atoms that do not buckle.

ing is strongly nonlinear and becomes zero for finite small buckling amplitude: therefore, merely having some buckling does not guarantee semiconducting behavior; instead some finite threshold value must be crossed.

For convenience, we will focus on $(n,0)$ nanotubes. As Fig. 12 demonstrates for the example of the (5,0) nanotube, all buckling atoms in a $(n,0)$ nanotube lie on rings about the circumference on the nanotube. Any given ring can be classified by one of three labels: (i) the ring contains inward buckling atoms, (o) the ring contains outward buckling atoms, or (-) the ring does not contain buckling atoms. For the two ground states, the sequence is either the repeated "io-" pattern or the repeated "oi-" pattern. An abrupt soliton going from one to the other minimum is denoted by "…io-io-oi-oi-…." Of course, the transition region joining the io- and oi-minima will generally have some width in order to lower the energy as we detail below.

We extract soliton energies from first principles calculations as follows. For the (3,0) and (5,0) nanotubes, we chose unit cells that were two or three times the respective primitive cell. Starting from the repeated io- ground state, we created abrupt solitons of the "io-oi" and "oi-io" variety by fixing the buckling atoms into the appropriate positions and relaxing all other atomic coordinates. Due to periodic boundary conditions, two equivalent solitons are created in the unit, one io-oi and the other oi-io. To allow for wider solitons, we allowed some of the buckling atoms to relax: for example, for a triple-long nanotube, starting from the abrupt "io-io-io-oi-oi-oi" state, we relaxed to the "io-io-xx-oi-oi-xx" configuration where all the atoms in the rings denoted by "x" are allowed to fully relax. An even wider soliton would be io-xx-xx-oi-xx-xx. Table VI contains our first principles LDA results for the energies of the various soliton configurations. Widening the solitons does reduce the energy but the reduction is most significant when the first pair of buckled rings is allowed to relax. This data suggests that the solitons would be at most four buckling rings wide.

To help us model longer unit cells and other $(n,0)$ nanotubes, we fit our results to a simple model. First, we note that the buckling configuration is specified by the amplitude of a unit of three neighboring rings. For example, io- has optimal positive buckling, oi- has optimal negative buckling, and xx- has an intermediate value. Let j index each such three ring unit and A_j be its buckling amplitude. The LDA calculations on a primitive cell of a nanotube provide us with the energy $\mathcal{E}_{coh}(A)$ of coherently buckling the entire length of the nanotube by amplitude A: this is what is shown in Fig. 10 and 11. When there are fluctuations in buckling, in addition to energy changes due to the fact that $\mathcal{E}_{coh}(A)$ depends on A, there will also be energy costs due to the nonuniformity of A_j along the nanotube, which we model by a nearest-neighbor spring model. Thus our model is

$$E_{tot} = \sum_j \mathcal{E}_{coh}(A_j) + \frac{K}{2}(A_{j+1} - A_j)^2, \tag{9}$$

where K is the spring constant for A_j variations along the length. Using this model together with the *ab initio* data of Table VI and the actual A_j values from the associated struc-

TABLE VI. LDA energy costs for soliton configurations of (3,0) and (5,0) single-walled A(1/9)-derived nanotubes. The "Configuration" column describes the unit cell used and its geometry (see text for the "i," "o," "-," and "x" nomenclature). E_{sol} is the energy per soliton in eV above the ground-state for that configuration. K is the extracted spring constant for the simplified model of Eq. (9) in eV/Å^2.

Nanotube	Configuration	E_{sol}	K
(3,0)	io-io-io-io	0	
(3,0)	io-io-oi-oi	1.25	1.89
(3,0)	io-xx-oi-xx	0.86	1.79
(3,0)	io-io-io-io-io-io	0	
(3,0)	io-io-io-oi-oi-oi	1.39	2.04
(5,0)	io-io-io-io	0	
(5,0)	io-io-oi-oi	0.92	2.28
(5,0)	io-xx-oi-xx	0.60	1.98
(5,0)	io-io-io-io-io-io	0	
(5,0)	io-io-io-oi-oi-oi	0.96	2.58
(5,0)	io-io-xx-oi-oi-xx	0.64	2.34
(5,0)	io-xx-xx-oi-xx-xx	0.57	2.39

tures, we back out K for each case and list them in Table VI. Despite the simplicity of the model, there is a general agreement for the extracted K: $K \approx 1.8$ eV/Å^2 for the (3,0) nanotube and $K \approx 2.3$ eV/Å^2 for the (5,0) nanotube. Based on this, we assume that $K \approx 2$ eV/Å^2 is a reasonable value of K for all $(n,0)$ nanotubes. To extend this model to all $(n,0)$ nanotubes, we observe that the function $\mathcal{E}_{coh}(A)$ for the (3,0) and (5,0) nanotubes is fit quite accurately by a fourth-order polynomial $\mathcal{E}_{coh}(A)=E_{coh}(0)+gA^2+hA^4$; we extract the two constants g and h by reproducing the two important data for each $(n,0)$ nanotube in Table V: that the minima occur at $A=\pm A_{buckle}$ and that the buckled configurations at $\pm A_{buckle}$ are δE lower in energy than the flat one at $A=0$.

Solving for solitons of the energy function of Eq. (9) is straightforward. We consider a 100 long chain of rings, constrain the left 30 to be in the io- configuration, the right 30 to be in the oi- configuration, and relax the interior 40 rings to minimize E_{tot}. The resulting solitons turn out to be quite narrow, typically 2–4 buckling rings at most. The resulting energies per soliton from this model for a range of $(n,0)$ nanotubes is shown in Table VII. We note that the LDA-based soliton energies are smaller than the GGA-based ones simply because, as Table V shows, the LDA predicts a smaller energy difference between the flat and buckled configuration and a smaller buckling amplitude.

The results in Table VII show that even at room temperature, the average spacing between solitons—given by $\exp(E_{sol}/k_BT)$ lattice spacings—is quite large even for the semiconducting (8,0) nanotube within LDA: for the (8,0), the average soliton-soliton spacing is some 200 unit cells. Although solitons are much more closely spaced for the (10,0) or larger tubes, these are already metallic nanotubes (see Table V). Therefore, the soliton fluctuations are sparse enough that, for the nanotubes with semiconducting ground states, most of the nanotube length in practice will be composed of semiconducting regions separated by rare and narrow metallic segments.

TABLE VII. Soliton energies for the $(n,0)$ nanotubes in eV/soliton based on the model of Eq. (9) with $K=2$ eV/Å^2. The predictions based on LDA and GGA are presented separately.

	LDA	GGA
Nanotube	E_{sol}	E_{sol}
(3,0)	0.73	0.97
(4,0)	0.62	0.85
(5,0)	0.50	0.75
(6,0)	0.36	0.62
(8,0)	0.14	0.50
(10,0)	0.001	0.003

The model of Eq. (9) also allows us to estimate the effect of thermal fluctuations about each buckled configuration on the band gap of the nanotube: Figs. 10 and 11 show that as the buckling amplitude fluctuates about its minimum value, the band gap values for the nanotube generally decrease since they are close to maximal at the optimal buckling configuration. However, classical Monte Carlo sampling using Eq. (9) reveals that the fluctuations for the semiconducting nanotubes—even up to (8,0)—only create a modest reduction in the average band gap value during the sampling.

Summarizing this section, we find that although thermal or soliton fluctuations are possible, the energetics of the semiconducting single-walled nanotubes prevent them from modifying the nanotube electronic properties significantly from those of the predicted ground-state structures. Namely, even including thermal fluctuations at room temperature, the single-walled nanotubes that are predicted to have a semiconducting ground state should in fact be semiconducting over most of their lengths.

VI. DOUBLE-WALLED BORON NANOTUBES

Although single-walled boron nanotubes show very interesting properties such as a metal-insulator transition versus tube diameter, given that double-layered boron sheets are more stable than single-layered ones, we should consider the question of whether single- or double-walled nanotubes are the proper ground state for boron nanotubes of small to medium diameter. As per Sec. IV, the double-Z(1/12) sheet is 0.135 eV/atom more stable than the most stable single-layered A(1/9) sheet. Thus, large-diameter double-walled nanotubes made of double-Z(1/12) are guaranteed to be more favorable than single-walled ones. However, smaller diameter double-walled nanotubes have large curvatures which make it harder to predict the structure and properties ahead of time.

The aim of this section is to study the structures, energetics and electronic properties of double-walled boron nanotubes and to compare them to single-walled ones as a function of diameter. Here, we will consider three classes of double-walled nanotubes: (a) the most obvious structures are

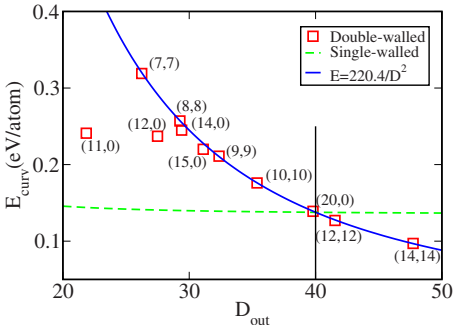

FIG. 13. (Color online) Red squares are the curvature energies E_{curv} (in eV/atom) versus outer wall diameter D_{out} (in Å) for double-walled nanotubes made from rolling the double-Z(1/12) sheet. The blue solid line is the result of a $1/D_{out}^2$ fit to all the data excluding the anomalous (11,0) and (12,0) cases (those two show structural collapse due to high curvature as per Fig. 14). The green dashed line shows the curvature energies for single-walled A(1/9)-derived nanotubes with an added constant energy of 0.135 eV/atom to account for the energy difference between the A(1/9) and double-Z(1/12) sheets. The two curves cross at $D_{out} \approx 40$ Å. All data are calculated using SIESTA with the LDA approximations.

obtained by creating double-walled nanotubes by rolling up the highly stable double-Z(1/12) sheet as it is; (b) double-walled nanotubes made from two coaxial single-walled A(1/9)-derived nanotubes of different diameters; and (c) double-walled nanotubes constructed from coaxial single-walled Z(1/12)-derived nanotubes of different diameters. Clearly, these three do not exhaust all the possibilities for double walled nanotubes but we believe that they form a reasonable set of structures to study for an initial orientation and investigation and have a high chance of including the actual ground-state structure for double-walled boron nanotubes.

A. Double-walled nanotubes from the double-Z(1/12) sheet

We first consider double-walled boron nanotubes constructed by rolling up the most stable double-layered Z(1/12) sheet. Although this sheet is the most stable in our library, the nanotube is expected to be quite stiff under curvature compared to any single-layered case because its inner and outer walls have the same number of atoms but are geometrically forced to have different diameters (radii of curvature) which stretches the outer surface, compresses the inner surface, and strains the interlayer bonds. Figure 14 shows two examples of such nanotubes.

First-principles results support this expectation. Figure 13 shows the curvature energy versus outer nanotube diameter for such double-walled nanotubes. The curvature energies are about an order of magnitude larger than those of carbon nanotubes and single-walled boron nanotubes of the same diameter. It turns out that due to the very high curvatures, some of the bonds on the outer surfaces of the smallest-diameter double-walled nanotubes of this class break to release tension. As shown in Fig. 14, many boron-boron bonds in the outer surface of the (12,0) nanotube are broken forming "holes" on that surface, while for the (20,0) nanotube, the

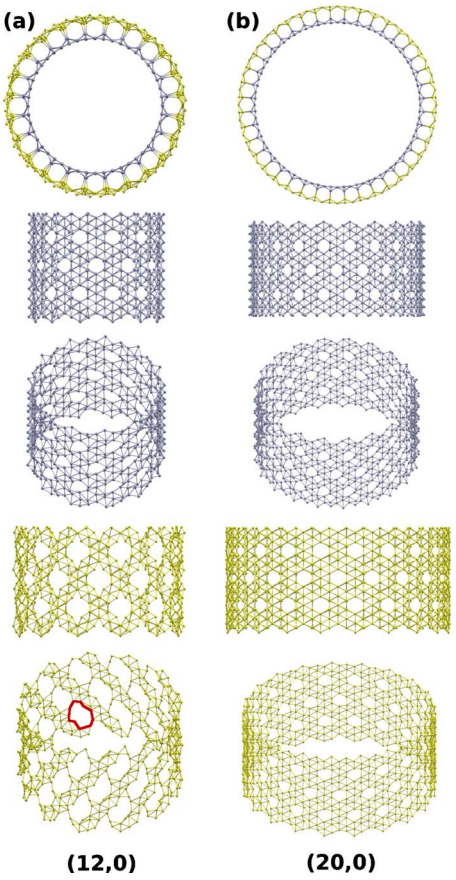

FIG. 14. (Color online) Structures of nanotubes (a) (12,0) and (b) (20,0) made of the double-Z(1/12) sheet. The top row shows the structure of each nanotube viewed down its axis. In the next four rows, we show the geometry of the inner and outer walls (surfaces) separately: the second and third row show a side and angled view of the inner surface, and the fourth and fifth rows show the side and angled view of the outer surface. To help the reader, inner surface atoms are shown in gray (darker) while outer surface atoms are shown in yellow (lighter). In the fifth row, red solid lines mark an example of a structural "hole" that is formed for the (12,0) nanotube on its outer surface due to broken boron-boron bonds.

outer surface has the same geometry as the Z(1/12) sheet with no broken bonds. For the smallest diameter nanotubes we have considered of this class, namely, (11,0) and (12,0), this strain release mechanism tends to reduce the curvature energies below the expected elastic trend of a $1/D_{out}^2$ behavior (see Fig. 13). Electronically, all the double-walled nanotubes without broken bonds on the outer walls are semiconducting, as expected from the semiconducting nature of the parent double-Z(1/12) sheet.

After excluding the anomalous (11,0) and (12,0) cases, we can fit the remaining data in Fig. 13 corresponding to $D_{out} > 25$ Å very well with the standard elastic formula of Eq. (8). We obtain $C = 220$ eV Å^2/atom. This is about 50 times larger than the corresponding value for single-walled A(1/9)-derived nanotubes. By accounting for the 0.135 eV/atom difference in energy between the A(1/9) sheet and the double-Z(1/12) sheet, we find a crossover in stability from single-walled to double-walled at a diameter of $D_{out} \approx 40$ Å. Hence, if we only compare these two classes of nanotubes,

TABLE VIII. Binding energy in eV/atom of double-walled boron nanotubes made from two distinct coaxial single-walled A(1/9) nanotubes (calculated by SIESTA with the LDA approximation). We only consider cases where both inner and outer tubes are both of $(n,0)$ (up panel) or (n,n) (bottom panel) variety. Larger binding energies correspond to more stable structures.

		Outer $(n,0)$						
		12	11	10	9	8	7	6
Inner $(m,0)$	10	7.37						
	9	7.42	7.36					
	8	7.40	7.42	7.33				
	7	7.39	7.40	7.42	7.32			
	6	7.37	7.39	7.39	7.42	7.37		
	5	7.36	7.36	7.38	7.40	7.41	7.37	
	4	7.35	7.35	7.35	7.37	7.40	7.40	7.33
	3	7.34	7.33	7.33	7.33	7.35	7.35	7.38
		Outer (n,n)						
		8	7	6	5	4		
Inner (m,m)	7	7.41						
	6	7.43	7.40					
	5	7.40	7.43	7.39				
	4	7.37	7.39	7.45	7.39			
	3		7.36	7.38	7.43	7.39		
	2			7.35	7.36	7.43		

we would have the following progression: the ground-state is double-walled and semiconducting for $D>40$ Å and single-walled for $D<40$ Å; as per the previous section, for $20<D<40$ Å, the single-walled tubes are metallic and for $D<20$ Å they are semiconducting.

B. Double-walled nanotubes from two A(1/9) sheets

As we saw above, although double-Z(1/12) is the most stable sheet, its large curvature energy makes it unfavorable for small diameter nanotubes. The large curvature cost is due to the fact that we are constructing double-walled nanotubes by using two identical sheet segments to construct the inner and outer walls. This in turn causes a great deal of strain as neither surface can be optimized.

Obviously, one can reduce the strain greatly by constructing double-walled nanotubes with inner and outer surfaces of differing diameters. Although one can attempt to choose inner and outer surfaces (i.e., single-walled nanotubes) that are each optimal separately, when putting them together to make a double-walled structure, one will sacrifice the optimal bonding between the two that was guaranteed in the sheet structure when both were the same sheet. Therefore, *a priori* it is not obvious in which diameter regimes such a program will be successful and we must rely on first principles results to provide guidance. This situation is directly analogous to multiwalled carbon nanotubes[63] but with the added complication that for boron strong interwall chemical bonds can form. This section and the next investigate the properties of double-walled nanotubes constructed from different-sized inner and outer single-walled nanotubes.

To begin, we will focus on double-walled nanotubes made from two single-walled A(1/9)-derived nanotubes. The rationale is that the A(1/9) sheets normally do not form strong interlayer bonds so that we may avoid or at least minimize the complication due to interlayer bonding. Our approach to finding optimal double-walled structures is the following: for a fixed chosen outer single-walled nanotube, we choose a number of inner nanotubes, perform full relaxations of the resulting double-walled structures, and locate the lowest-energy resulting combination. We then tabulate our results as a function of the outer tube. Although other schemes are imaginable, we choose the outer diameter as the independent variable primarily because current methods for fabrication of boron nanotubes[25] (as well as some nonboron nanotube growth methods) use a hollow cylindrical physical template inside of which the nanotube is constrained to grow. Thus the exterior diameter is the variable most obviously constrained by the experimental setup.

We label these double-walled nanotubes in the following manner: we provide the name of the sheet used to create the nanotubes followed by a pair of (n,m) labels specifying the outer and then inner nanotube. Therefore, A(1/9)-(8,0)-(4,0) refers to a double-walled nanotube constructed from the (8,0) and (4,0) single-walled A(1/9)-derived nanotubes. For computational convenience, we only consider double-walled tubes where inner and outer nanotubes are both $(n,0)$ or both (n,n): this means both single-walled nanotubes are commen-

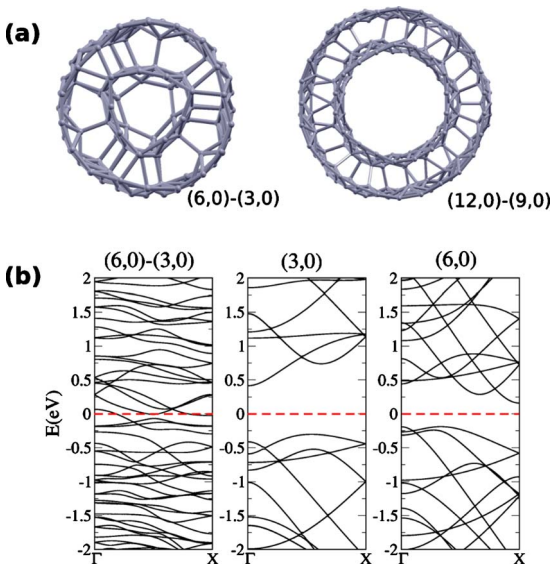

FIG. 15. (Color online) (a) Atomic geometries of the double-walled boron nanotubes A(1/9)-(6,0)-(3,0) and A(1/9)-(12,0)-(9,0) viewed down the nanotube (z) axis. See text for nomenclature. (b) LDA band structure of the double-walled A(1/9)-(6,0)-(3,0) nanotube compared to the constituent single-walled (3,0) and (6,0) cases. In all cases, the energies are shifted so that the Fermi energies are at zero.

surate and thus we can model the double-walled tubes using periodic boundary conditions with relatively small periodic unit cells along the nanotube axis.

Table VIII presents the binding energy as a function of various inner-outer pairings for A(1/9)-(n,0)-(m,0) and A(1/9)-(n,n)-(m,m) double-walled nanotubes. For both groups, the tabulated data shows that the optimal combinations are A(1/9)-(n,0)-(n-3,0) and A(1/9)-(n,n)-(n-2,n-2). Geometrically, we find that bonds form between the inner and outer walls in all the cases studied here. Figure 15 shows two such examples. The interwall bond lengths are in the range of 1.7–1.9 Å. The distances between the walls of inner and outer nanotubes are 2.8–3.2 Å for A(1/9)-(n,0)-(m,0)-type and 3.2–3.6 Å for A(1/9)-(n,n)-(m,m)-type double-walled nanotubes, which are close to the interlayer distance of 3.49 Å in the double-A(1/19) sheet (see Table III). Electronically, the formation of the interwall bonds changes the buckling pattern on both inner and outer surfaces and renders all the double-walled nanotubes investigated here metallic. For example, Fig. 15 shows the relevant band structures in the case of A(1/9)-(6,0)-(3,0): the double-walled nanotube has multiple bands crossing the Fermi energy even though the individual constituent (3,0) and (6,0) nanotubes are semiconducting separately.

We note that our results are restricted to relatively small diameter double-walled nanotubes which have relatively large curvatures: the largest nanotube in our library is A(1/9)-(18,0)-(15,0), which has an outer diameter of 28.9 Å and still has interwalled bonds formed between inner and outer nanotubes. Although we are presently unable to directly verify the properties of larger diameter double-walled nanotubes through explicit calculations, we can make some general arguments. For very large diameters, we expect weak curvature which means each nanotube is quite close to being a flat A(1/9) sheet. As described in Sec. IV, two A(1/9) sheets stay flat and apart at a distance of 3.49 Å and do not form chemical bonds. Therefore, such large diameter double-walled boron nanotubes will be similar to double-walled carbon nanotubes in that there will be weak van der Walls interactions between the walls. We would expect the interwall distance to be quite close to 3.49 Å. This fixed distance (i.e., fixed diameter difference) allows us to estimate that the optimal combinations for large diameters will be A(1/9)-(n,0)-(n-4,0) and A(1/9)-(n,n)-(n-2,n-2) for (n,n). Notice that the optimal combination for large-diameter (n,0) type nanotubes is different from small-diameter ones. Electronically, we expect such double-walled nanotubes to be metallic since each individual constituent single-walled nanotube is metallic by itself.

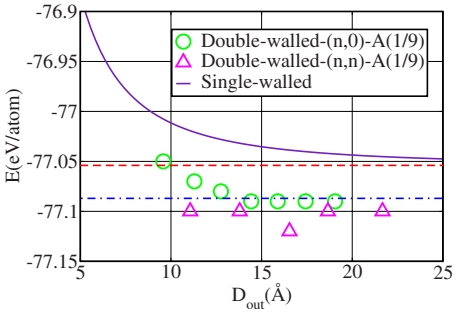

FIG. 16. (Color online) Total energies (from LDA) per atom versus outer diameter D_{out} for single-walled A(1/9)-derived nanotubes (solid indigo curve), double-walled A(1/9)-(n,0)-(n-3,0) for n=6–12 (green circles), and double-walled A(1/9)-(n,n)-(n-2,n-2) for n=4–8 (magenta triangles). The red dashed line is the energy of a single flat A(1/9) sheet. The blue dot-dash straight line shows the energy of the double-A(1/9) sheet.

We now compare the stability of these double-walled boron nanotubes to the A(1/9)-derived single-walled ones. Figure 16 shows the total energy per atom versus outer diameter for these two classes of nanotubes. In all cases studied here, the double walled are more stable than the single-walled variety, typically by 0.05 eV/atom. As the Figure shows, the energies in both cases have essentially asymptoted to the respective sheet energies so we expect this relative stability to also hold for larger diameters. We note that the energy of large diameter double-walled nanotubes asymptotes to the energy of the double-A(1/9) sheet which is some 0.03 eV/atom more stable than the single-walled A(1/9) sheet due to weak intersheet interactions. There appears to be some chirality dependence to the data as the A(1/9)-(n,n)-(n-2,n-2) are lower in energy than the A(1/9)-(n,0)-(n-3,0) but at present we do not have a detailed understanding of this difference. In brief, this section shows that for all diameters envisioned, double-walled A(1/9)-derived nanotubes will be more stable than their single-walled varieties. Furthermore, we expect all the A(1/9)-derived double-walled nanotubes to be metallic.

C. Double-walled nanotubes from two Z(1/12) sheets

We just have shown that double-walled nanotubes constructed from the A(1/9) sheet are always more stable than

TABLE IX. Binding energy in eV/atom of double-walled boron nanotubes made from two coaxial single-walled Z(1/12) nanotubes (calculated by SIESTA with the LDA approximation). We only consider cases where both inner and outer tubes are $(n,0)$ (left) or (n,n) (right) type. Larger binding energies correspond to more stable structures.

		Outer $(n,0)$				
		10	9	8	7	6
Inner $(m,0)$	8	7.44				
	7	7.49	7.45			
	6	7.43	7.47	7.43	7.27	
	5		7.41	7.47	7.42	7.28
	4			7.40	7.49	7.43
	3			7.32	7.41	7.47

		Outer (n,n)			
		8	7	6	5
Inner (m,m)	7	7.41			
	6	7.51	7.40		
	5	7.35	7.49	7.40	
	4	7.33	7.34	7.48	7.43
	3		7.33	7.33	7.47
	2			7.31	7.32

single-walled ones for all diameters. Since the double-Z(1/12) sheet is more stable than the double-A(1/9) sheet (see Table III), we might further stabilize double-walled nanotubes by pairing two coaxial single-walled Z(1/12) nanotubes of different diameters.

We follow the same program as in the previous section for the A(1/9)-derived double-walled nanotubes when constructing double-walled structures. Again, for simplicity, we consider only the cases where both inner and outer nanotubes are both $(n,0)$ or both (n,n). We employ the same nomenclature as the previous section so that Z(1/12)-(n,m)-(p,q) is a double-walled nanotube with outer single-walled tube (n,m) and inner single-walled tube (p,q) and where both single-walled nanotubes are made from curving a Z(1/12) sheet.

Table IX presents the binding energy for different combinations of inner and outer nanotubes. The optimal combinations are $(n,0)$-$(n$-3,0) and (n,n)-$(n$-2,n-2). Figure 17 shows the structures of Z(1/12)-(9,0)-(6,0) and Z(1/12)-(8,8)-(6,6). In all cases we have studied in this work, as exemplified by Fig. 17, we find that interlayer bonds form between the inner and outer surfaces with a bond length close to 1.7 Å. The fact that such bonds form is of no surprise since the double-Z(1/12) sheet has interlayer bonds of the same length. However, the number of bonds formed is harder to predict: since the inner and outer tubes have different number of atoms, no all the bonds that form in the sheet geometry are possible in the tube geometry. More careful examination shows that the two classes of double-walled nanotubes solve this frustration in opposite manners: more intertube bonds than expected form for the Z(1/12)-$(n,0)$-$(n$-3,0) cases while too few bonds are formed in the Z(1/12)-(n,n)-$(n$-2,n-2) cases. Put another way, the Z(1/12)-$(n,0)$-$(n$-3,0) structures have the right number of bonds for the outer tube but too many for the inner tube, and the Z(1/12)-(n,n)-$(n$-2,n-2) have the oppo-

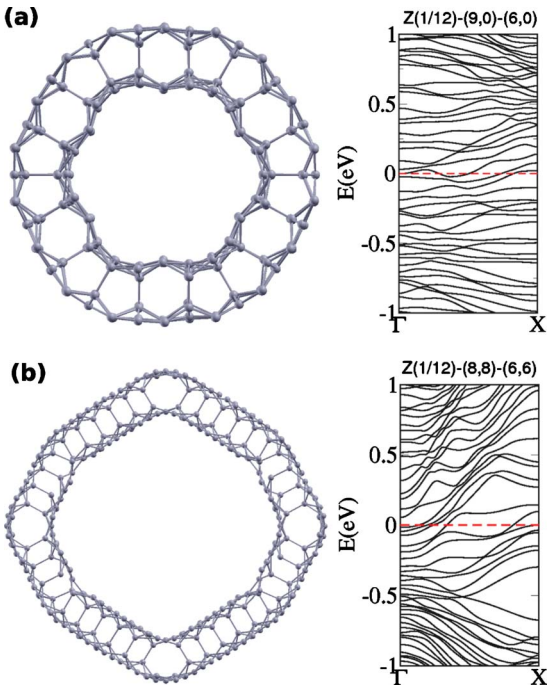

FIG. 17. (Color online) Atomic geometries viewed down the nanotube axis and LDA band structures for the (a) Z(1/12)-(9,0)-(6,0) and (b) Z(1/12)-(8,8)-(6,6) double-walled nanotubes. Fermi levels are at zero (energies are shifted accordingly) and denoted by the red horizontal dashed lines.

site behavior. This is visible in Fig. 17: for Z(1/12)-(9,0)-(6,0) we see a regular alternating buckling pattern on the outer wall whereas for Z(1/12)-(8,8)-(6,6) the inner wall features the alternative regular buckling.

The consequence of this "defective" interlayer bonding pattern on the electronic structure is that all such double-walled nanotubes we have studied are metallic. Figure 17 shows two examples of the band structures. This is different from the semiconducting nature of the double-Z(1/12) sheet or the double-walled nanotubes made directly from the double-Z(1/12) sheet of Sec. VI A. An analysis of the local densities of states of these small-diameter double-walled nanotubes shows that the states at the Fermi level are extended to the whole structure rather then being localized around the structural defects.

Due to computational limitations, the sample of double-walled nanotubes we present here from first principles is limited to small diameters. Although we are not yet able to directly simulate larger diameter nanotubes, we can present general arguments to deduce their likely properties. Clearly, for very large diameters, in order to minimize the total energy, the local structure of such double-walled nanotubes will converge to the structure of the double-Z(1/12) sheet and the distance between the inner and outer walls will be close to 3.23 Å as appropriate to the double-layered sheet. This means that the optimal combinations will be $(n,0)$-$(n\text{-}3,0)$ and (n,n)-$(n\text{-}2,n\text{-}2)$ which are the same as found for the small diameter cases. Furthermore, since the inner walls have fewer atoms than the outer walls, the structural defects related to frustrated interlayer bonding persist for all large diameter double-walled nanotubes, and we thus expect them to be metallic as well. Quantitatively, the number of structural defects per unit nanotube length is constant for either $(n,0)$-$(n\text{-}3,0)$ or (n,n)-$(n\text{-}2,n\text{-}2)$ classes because the number of the defects is proportional to the constant difference in the number of atoms between inner and outer walls: the linear density of defects per unit length will not depend on diameter but only possibly on chirality.

We now turn to the comparative energetics for this class of double-walled nanotubes. Figure 18 shows the total energy per atom versus outer wall diameter for this class in comparison to those of the single-walled A(1/9)-derived nanotubes and the double-walled A(1/9)-derived nanotubes. For the range of diameters examined, double-walled nanotubes made from two coaxial Z(1/12) single-walled nanotubes are always the most stable. As discussed in Sec. VI A, single-walled A(1/9)-derived nanotubes are more stable than double-walled nanotubes rolled up directly from the double-Z(1/12) sheet for $D_{out}<40$ Å. Therefore, at least for $D_{out}<40$ Å, metallic double-walled nanotubes constructed from two different concentric Z(1/12) single-walled nanotubes are our best candidate for the ground-state structure.

To predict the ground state for $D_{out}>40$ Å, we compare the metallic double-walled nanotubes made from two different concentric Z(1/12) single-walled nanotubes with the semiconducting ones based on the double-Z(1/12) sheet. From Sec. VI A, the latter group has an energy per atom given by

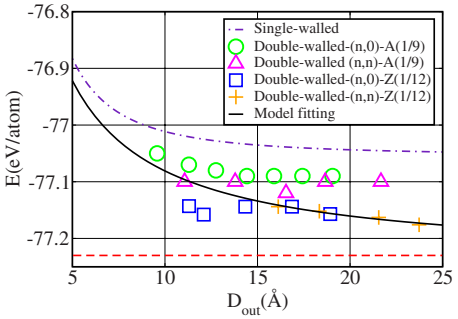

FIG. 18. (Color online) Total energies (from LDA) per atom versus outer diameter D_{out} for single-walled boron nanotubes (indigo dot-dash line), double-walled boron nanotubes made of A(1/9) single-walled nanotubes (green circles and magenta triangles), and double-walled boron nanotubes from two Z(1/12) single-walled nanotubes (blue squares and yellow plus). The red dashed line shows the energy of the double-Z(1/12) sheet. The black solid curve is a fitting to squares and plus in the range of 15 Å $<D_{out}<25$ Å.

$$E = E[\text{double-Z}(1/12)] + (220.4\ \text{eV Å}^2)/D_{out}^2, \quad (10)$$

where $E[\text{double-Z}(1/12)]$ is the energy per atom for the double-Z(1/12) sheet. For the former group, when tube diameter becomes very large, they are essentially gently curved double-Z(1/12) sheets with a fixed number of structural defects per unit length. So the total energy has two important contributions: the total energy per atom of the double-Z(1/12) sheet and the energy increase due to the structural defects—the curvature energy is minimized by choosing optimal choice of inner and outer walls and we assume it can be neglected (if it were to be included it would be a small subleading term of order $1/D_{out}^2$). Since the number of defects per unit length is constant regardless of tube diameter, we assume that each defect increases the total energy by a constant amount, which when divided by the number of atoms, gives a contribution proportional to $1/D_{out}$. So we expect the total energy for large diameters to be given approximately by

$$E = E[\text{double-Z}(1/12)] + S/D_{out} \quad (11)$$

for some constant S. We fit the available data in Fig. 18 for 15 Å $<D_{out}<25$ Å and find $S=1.59$ eV Å. Comparing the above two formula gives a crossing at $D_{out}=139$ Å. Therefore, we can safely state that for the experimentally fabricated range of nanotubes with $D_{out}<100$ Å,[25] our best candidates for the ground state are double-walled boron nanotubes constructed from two different concentric Z(1/12) single-walled nanotubes. All such nanotubes are computed to be or are expected to be metallic.

VII. SUMMARY AND OUTLOOK

In summary, we have presented work on the structures, energetics, and electronic properties of single- and double-layered boron sheets and single- and double-walled boron nanotubes. For the single-layered sheets, we have studied the very common buckling behavior seen in clusters, sheets, and

nanotubes. We have demonstrated that the buckling is driven primarily by kinetic energy reduction and that buckling has a similar effect to reducing the average electron density. For double-layered sheets, their stability and structures are closely related to the buckling behavior of the parent single-layered sheets: creating double-layered sheets from single-layered sheets that prefer to buckle will lead to the formation of stabilizing bonds between the two sheets. The most stable boron sheet we have found is made of two $\eta=1/12$ single-layered sheets [double-Z(1/12)], is more stable than any single-layered sheet, and is semiconducting. We note that $\eta=1/12$ is smaller than that of the most stable single-layered sheet A(1/9) with $\eta=1/9$.

For nanotubes, we have begun with single-walled nanotubes made from the most stable single-layered A(1/9) sheet. We show that the energy lowering due to surface buckling that makes them semiconducting turns out to be very small and we caution in quantitative use of small energy differences that may not be very accurate within LDA or GGA. However, we believe the trend to be correct: that the surface buckling and the gap decrease with increasing nanotube diameter and vanish beyond diameters of ~20 Å. Furthermore, we show that the semiconducting gap is robust: the nanotubes predicted to be semiconducting in the ground state should actually be semiconducting over most of their lengths when finite temperature fluctuations are considered.

For multiwalled nanotubes, we have focused only on double-walled varieties in this work. We have investigated a variety of double-walled nanotubes made from various pairings of single-walled inner and outer nanotubes. Generally, unlike double- or multiwalled carbon nanotubes, double-walled boron nanotubes can be strongly stabilized by the formation of chemical bonds between the inner and outer walls. The most stable structure we have found is made from two singled-walled Z(1/12) sheets of different sizes, where the sizes are chosen mainly to minimize the strain due to curvature. These double-walled nanotubes are predicted to be metallic up to diameters of 100 Å which covers the experimentally relevant size range at present.[25] [Beyond that, nanotubes made directly from rolling the double-Z(1/12) sheet are more stable and are semiconducting.] Again, we note that the most stable double-walled nanotubes have walls (surfaces) with η smaller than the stable single-walled varieties.

Although we have not investigated multiwalled nanotubes with three or more layers, we may speculate that with proper choices of constituent sheets making up the walls, interwall bonds will form to stabilize the overall structure. In principle, one can imagine this process continuing leading to highly stable boron nanotubes with very many walls. However, the available experimental transmission-electron-microscopy images[25] show that the actual fabricated nanotubes are hollow in the center. If the ground-state structures of boron nanotubes have many walls, this raises the complex question of at what point kinetic limitations during the growth limit the available structures sampled during the fabrication. Therefore, we believe that better understanding of the experimental growth kinetics and their implications on the fabricated structures are necessary for a proper modeling and understanding of the properties of boron nanotubes.

ACKNOWLEDGMENTS

This work was primarily supported by the National Science Foundation under Contract No. DMR-0808665 and partially through TeraGrid resources provided by NCSA-Abe under Grant No. TG-MCA08X007. We thank the Bulldog parallel computer clusters of the Yale High Performance Computing center for providing the remaining computational resources.

[1] M. Fujimori, T. Nakata, T. Nakayama, E. Nishibori, K. Kimura, M. Takata, and M. Sakata, Phys. Rev. Lett. **82**, 4452 (1999).
[2] N. Vast, S. Baroni, G. Zerah, J. M. Besson, A. Polian, M. Grimsditch, and J. C. Chervin, Phys. Rev. Lett. **78**, 693 (1997).
[3] S. Shang, Y. Wang, R. Arroyave, and Z.-K. Liu, Phys. Rev. B **75**, 092101 (2007).
[4] T. Ogitsu, F. Gygi, J. Reed, Y. Motome, E. Schwegler, and G. Galli, J. Am. Chem. Soc. **131**, 1903 (2009).
[5] A. R. Oganov, J. Chen, C. Gatti, Y. Ma, C. W. Glass, Z. Liu, T. Yu, O. O. Kurakevych, and V. L. Solozhenko, Nature (London) **457**, 863 (2009).
[6] E. Y. Zarechnaya, L. Dubrovinsky, N. Dubrovinskaia, Y. Filinchuk, D. Chernyshov, V. Dmitriev, N. Miyajima, A. El Goresy, H. F. Braun, S. Van Smaalen, I. Kantor, A. Kantor, V. Prakapenka, M. Hanfland, A. S. Mikhaylushkin, I. A. Abrikosov, and S. I. Simak, Phys. Rev. Lett. **102**, 185501 (2009).
[7] I. Boustani, Chem. Phys. Lett. **233**, 273 (1995).
[8] I. Boustani, Chem. Phys. Lett. **240**, 135 (1995).
[9] I. Boustani, Surf. Sci. **370**, 355 (1997).
[10] I. Boustani, Phys. Rev. B **55**, 16426 (1997).
[11] H. J. Zhai, L. S. Wang, A. N. Alexandrova, and A. I. Boldyrev, J. Chem. Phys. **117**, 7917 (2002).
[12] H. J. Zhai, B. Kiran, J. L. Li, and L. S. Wang, Nature Mater. **2**, 827 (2003).
[13] H.-J. Zhai, A. N. Alexandrova, K. A. Birch, A. I. Boldyrev, and L.-S. Wang, Angew. Chem. Int. Ed. **42**, 6004 (2003).
[14] A. N. Alexandrova, A. I. Boldyrev, H. J. Zhai, and L. S. Wang, J. Phys. Chem. A **108**, 3509 (2004).
[15] B. Kiran, S. Bulusu, H. J. Zhai, S. Yoo, X. C. Zeng, and L. S. Wang, Proc. Natl. Acad. Sci. U.S.A. **102**, 961 (2005).
[16] J.-I. Aihara, H. Kanno, and T. Ishida, J. Am. Chem. Soc. **127**, 13324 (2005).
[17] I. Boustani, A. Quandt, and A. Rubio, J. Solid State Chem. **154**, 269 (2000).
[18] S. Chacko, D. G. Kanhere, and I. Boustani, Phys. Rev. B **68**, 035414 (2003).
[19] F.-Y. Tian and Y.-X. Wang, J. Chem. Phys. **129**, 024903 (2008).
[20] I. Boustani and A. Quandt, Europhys. Lett. **39**, 527 (1997).
[21] A. Gindulytė, W. N. Lipscomb, and L. Massa, Inorg. Chem. **37**, 6544 (1998).
[22] I. Boustani, A. Quandt, E. Hernandez, and A. Rubio, J. Chem. Phys. **110**, 3176 (1999).

[23] I. Boustani and A. Quandt, Comput. Mater. Sci. **11**, 132 (1998).
[24] A. Quandt and I. Boustani, ChemPhysChem **6**, 2001 (2005).
[25] D. Ciuparu, R. F. Klie, Y. Zhu, and L. Pfefferle, J. Phys. Chem. B **108**, 3967 (2004).
[26] M. H. Evans, J. D. Joannopoulos, and S. T. Pantelides, Phys. Rev. B **72**, 045434 (2005).
[27] J. Kunstmann and A. Quandt, Chem. Phys. Lett. **402**, 21 (2005).
[28] J. Kunstmann and A. Quandt, Phys. Rev. B **74**, 035413 (2006).
[29] K. C. Lau and R. Pandey, J. Phys. Chem. C **111**, 2906 (2007).
[30] I. Cabria, M. J. Lopez, and J. A. Alonso, Nanotechnology **17**, 778 (2006).
[31] A. Sebetci, E. Mete, and I. Boustani, J. Phys. Chem. Solids **69**, 2004 (2008).
[32] N. Gonzalez Szwacki, A. Sadrzadeh, and B. I. Yakobson, Phys. Rev. Lett. **98**, 166804 (2007).
[33] H. Tang and S. Ismail-Beigi, Phys. Rev. Lett. **99**, 115501 (2007).
[34] X. Yang, Y. Ding, and J. Ni, Phys. Rev. B **77**, 041402(R) (2008).
[35] Q.-B. Yan, X.-L. Sheng, Q.-R. Zheng, L.-Z. Zhang, and G. Su, Phys. Rev. B **78**, 201401(R) (2008).
[36] R. R. Zope, EPL **85**, 68005 (2009).
[37] R. R. Zope, T. Baruah, K. C. Lau, A. Y. Liu, M. R. Pederson, and B. I. Dunlap, Phys. Rev. B **79**, 161403(R) (2009).
[38] H. Tang and S. Ismail-Beigi, Phys. Rev. B **80**, 134113 (2009).
[39] A. K. Singh, A. Sadrzadeh, and B. I. Yakobson, Nano Lett. **8**, 1314 (2008).
[40] M. Li, Y. Li, Z. Zhou, P. Shen, and Z. Chen, Nano Lett. **9**, 1944 (2009).
[41] Y. Li, G. Zhou, J. Li, B.-L. Gu, and W. Duan, J. Phys. Chem. C **112**, 19268 (2008).
[42] P. Hohenberg and W. Kohn, Phys. Rev. **136**, B864 (1964).
[43] W. Kohn and L. J. Sham, Phys. Rev. **140**, A1133 (1965).
[44] M. C. Payne, M. P. Teter, D. C. Allan, T. A. Arias, and J. D. Joannopoulos, Rev. Mod. Phys. **64**, 1045 (1992).
[45] J. P. Perdew and A. Zunger, Phys. Rev. B **23**, 5048 (1981).
[46] J. P. Perdew, K. Burke, and M. Ernzerhof, Phys. Rev. Lett. **77**, 3865 (1996).
[47] N. Troullier and J. L. Martins, Phys. Rev. B **43**, 1993 (1991).
[48] PARATEC, (parallel total energy code) is a plane-wave pseudopotential program for parallel computations. http://www.nersc.gov/projects/paratec/
[49] PWSCF (plane-wave self-consistent field) is a computer code for electronic-structure calculations using pseudopotentials. http://www.pwscf.org/
[50] P. Giannozzi, S. Baroni, N. Bonini, M. Calandra, R. Car, C. Cavazzoni, D. Ceresoli, G. L. Chiarotti, M. Cococcioni, I. Dabo, A. D. Corso, S. de Gironcoli, S. Fabris, G. Fratesi, R. Gebauer, U. Gerstmann, C. Gougoussis, A. Kokalj, M. Lazzeri, L. Martin-Samos, N. Marzari, F. Mauri, R. Mazzarello, S. Paolini, A. Pasquarello, L. Paulatto, C. Sbraccia, S. Scandolo, G. Sclauzero, A. P. Seitsonen, A. Smogunov, P. Umari, and R. M. Wentzcovitch, J. Phys.: Condens. Matter **21**, 395502 (2009).
[51] P. Ordejón, E. Artacho, and J. M. Soler, Phys. Rev. B **53**, R10441 (1996).
[52] J. M. Soler, E. Artacho, J. D. Gale, A. Garcia, J. Junquera, P. Ordejon, and D. Sanchez-Portal, J. Phys.: Condens. Matter **14**, 2745 (2002).
[53] A. Kokalj, J. Mol. Graph. Model. **17**, 176 (1999).
[54] D. Porezag, T. Frauenheim, T. Köhler, G. Seifert, and R. Kaschner, Phys. Rev. B **51**, 12947 (1995).
[55] I. Boustani, A. Rubio, and J. A. Alonso, Chem. Phys. Lett. **311**, 21 (1999).
[56] R. Saito, G. Dresselhaus, and M. S. Dresselhaus, *Physical Properties of Carbon Nanotubes* (Imperial College Press, London, 1998).
[57] N. Hamada, S. I. Sawada, and A. Oshiyama, Phys. Rev. Lett. **68**, 1579 (1992).
[58] D. H. Robertson, D. W. Brenner, and J. W. Mintmire, Phys. Rev. B **45**, 12592 (1992).
[59] O. Gülseren, T. Yildirim, and S. Ciraci, Phys. Rev. B **65**, 153405 (2002).
[60] N. Gonzalez Szwacki and C. J. Tymczak, Chem. Phys. Lett. **494**, 80 (2010).
[61] C. Møller and M. S. Plesset, Phys. Rev. **46**, 618 (1934).
[62] T. Dauxois and M. Peyrard, *Physics of Solitons* (Cambridge University Press, Cambridge, 2006).
[63] S. Okada and A. Oshiyama, Phys. Rev. Lett. **91**, 216801 (2003).